FeS-cluster coordination of vertebrate thioredoxin regulates suppression of hypoxia-induced factor 2α through iron regulatory protein 1

Carsten Berndt[1]*, Eva-Maria Hanschmann[1,2,3], Laura Magdalena Jordt[2], Manuela Gellert[2], Leonie Thewes[1], Clara Ortegón Salas[2], Gereon Poschmann[4], Christina Sophia Müller[5], Yana Bodnar[2], Susanne Schipper[2], Oliver Handorf[2], Ricardo Nowack[6], Jean-Marc Moulis[7], Carola Schulzke[6], Volker Schünemann[5], and Christopher Horst Lillig[2]*

[1]Department of Neurology, Medical Faculty, Heinrich Heine University Düsseldorf, D-40225, Germany, [2]Institute for Biochemistry and Molecular Biology, University Medicine Greifswald, D-17475, Germany, [3]Department of Otorhinolaryngology, University Hospital Essen, D-45147, Germany, [4]Institute of Molecular Medicine, Proteome Research, Medical Faculty, Heinrich Heine University Düsseldorf, D-40225, Germany, [5]Department of Physics, University of Kaiserslautern-Landau, D-67663, Germany, [6]Institute of Biochemistry, University of Greifswald, D-17487, Germany, [7]Univ. Grenoble Alpes, CEA-IRIG and LBFA, Inserm U1055, Grenoble, F-38000, France

* correspondence:

Carsten Berndt, Department of Neurology, Medical Faculty, Heinrich Heine University, Moorenstr. 5, 40225 Düsseldorf, Germany, phone: +49 211 8105150, email: berndt@hhu.de

and

Christopher Horst Lillig, Institute for Medical Biochemistry and Molecular Biology, University Medicine Greifswald, Ferdinand-Sauerbruch-Strasse, 17475 Greifswald, Germany, phone: +49 3834 865407, email: horst@lillig.de

Abstract

Thioredoxins (Trxs) provide electrons to essential cellular processes such as DNA synthesis. Here, we characterize human and murine Trx1 as new iron-sulfur proteins. The [2Fe-2S] cluster is complexed using cysteinyl side chains 32 and 73 in a dimeric holo-complex. Formation of the holo-dimer depends on small structural changes of the loop connecting helices three and four and is stabilized by the formation of a direct interaction between Lys72 and Ser90 of two monomers. The not strictly conserved Cys73 in vertebrates co-evolved with the regulation of cellular iron homeostasis through the iron-regulatory proteins (IRP). Active apo-Trx1 is required for the reduction of cysteinyl residues in IRP1 and its binding to the iron-responsive element in the mRNA encoding hypoxia-inducible factor (HIF) 2α. Depletion of Trx1 increased the mRNA levels of HIF2α, an important target of IRP1. Hence, translation of the HIF2α mRNA requires either sufficient iron-supply or the lack of reducing power of the Trx system under iron-limiting conditions. Only then, HIF2α protein may accumulate under hypoxic conditions to transcriptionally regulate processes like erythropoiesis.

Keywords: hypoxia-inducible factor, iron-regulatory protein, iron metabolism, thioredoxin, iron-sulfur cluster

Significance Statement

Thioredoxins are, in general, cofactor-less key proteins in redox regulation and provide electrons to many essential cellular processes such as DNA synthesis. 50 years after its discovery, we show that mammalian thioredoxin 1 coordinates an iron-sulfur cluster using one of its active site cysteinyl residues and a non-conserved additional cysteinyl residue located outside the active site. This particular residue co-evolved with the vertebrate-specific iron regulatory system. Our study demonstrates that this system is regulated by thioredoxin 1 at the level of the iron-regulatory protein 1, thus linking redox and iron homeostases.

Introduction

Thioredoxin (Trx) is a small oxidoreductase catalyzing thiol-disulfide exchange reactions with two cysteinyl residues in its CxxC active site motif (overview in (1)). Trxs are reduced by the dedicated NADPH-dependent flavo- and selenoenzyme Trx reductase (TrxR). Mammalian cells contain two pairs of Trx/TrxRs, *i.e.* cytosolic Trx1/TrxR1 and mitochondrial Trx2/TrxR2. Trxs were first described as electron donors for ribonucleotide reductase (2). Today, however, Trxs are better known as major regulators of various cellular functions through the redox-regulation of thiol-disulfide switches and other redox modifications in key proteins (3, 4).

Cellular functions, especially redox-controlled functions, depend on the presence of specific organic or inorganic cofactors. Among inorganic cofactors, iron has a prominent role as it can be incorporated *e.g.* as heme or iron-sulfur (FeS) center into proteins. These proteins are essential to facilitate transport of oxygen or electron transfer reactions, for instance in the respiratory chain, DNA replication and repair, mRNA translation and cellular metabolism (5). Iron deficiency can lead to anemia, iron overload can induce cellular toxicity and is associated with various pathologies. Frequently, these can be traced back to the formation of hydroxyl radicals via the so-called Fenton reaction, see for instance (4, 6). Because cellular iron levels need to be tightly controlled, organisms have developed effective mechanisms for iron regulation. Whereas lower organisms utilize transcriptional regulation to control iron homeostasis, vertebrates have developed a post-transcriptional mechanism via iron regulatory proteins (IRPs) (7–9) at the cellular level that complements systemic regulations. Activities of IRP1 and IRP2 are regulated in different ways. IRP1 is active under iron deficiency, when its [4Fe-4S] cofactor is lost; the holo-protein functions as aconitase. Thus, the FeS cluster in IRP1 is considered to have an iron-sensing function (8). For RNA binding, cysteines of IRP1 needs to be in a reduced state (10). Activity of IRP1 after nitrosylation, a cysteine modification, can be restored by Trx1 (11). IRP2 on the other hand has not been demonstrated to bind an FeS cluster and is regulated via

ubiquitinylation and proteasomal degradation. Ubiquitination depends on the F-box/LRR-repeat protein 5 (FBXL5), whose stability depends on a di-iron center (12, 13). IRPs 1 and 2 bind to specific mRNA structures, called iron responsive elements (IREs), for instance of the iron import protein transferrin receptor (TfR), the iron storage protein ferritin, and the iron export protein ferroportin. Since approximately ten years it has been known that also the 5´UTR of hypoxia inducible factor 2α (HIF2α) mRNA contains an IRE (14, 15). Although both IRPs are able to bind this IRE (14), *in vivo* experiments suggest that IRP1 dominates the suppression of HIF2α mRNA translation under iron-limiting conditions (14–18).

HIF2α is a critical part of the hypoxic response signaling pathway. In the presence of oxygen, the alpha subunits of all hypoxia-inducible factors are hydroxylated at conserved proline residues by specific HIF prolyl-hydroxylases. These hydroxylated forms are flagged for proteasomal degradation by the von-Hippel-Lindau E3 ubiquitin ligase (19). In the absence of oxygen, *i.e.* hypoxia, hydroxylation fails and the proteins translocate into the nucleus where they act as transcription factors. HIF2α controls, most importantly, erythropoiesis (20) and the growth and progression of various forms of cancer (21).

Redox regulation, iron homeostasis, and the hypoxic response strongly depend on each other. Until now, however, mechanistic insights into these crosstalks are sparse. Here, we show, that human and murine cytosolic Trx1s coordinate a $[2Fe\text{-}2S]^{2+}$ cluster and explain the structural changes allowing the coordination of the cofactor. The loss of this FeS center activates the thiol-disulfide oxidoreductase activity of the protein. Active Trx1 is required for the reduction of cysteinyl residues in apo-IRP1, a prerequisite for their binding to IREs. The suppression of HIF2α translation under hypoxic – but iron-limited – conditions depends critically on the reductive capacity of the cytosolic Trx1/TrxR1/NADPH system.

Results

During regular purification of recombinant Trxs expressed in *E. coli*, we noted a distinct brown-yellowish color of the human and mouse Trx1 proteins.

Mammalian Trx1s complex a [2Fe-2S]$^{2+}$ cluster

The UV-Vis spectra of the recombinant human and mouse proteins freshly purified from *E. coli* cultures display two peaks at approx. 335 and 420 nm, in addition to the peak of the aromatic side chains at 280 nm (Fig. 1A). These absorption features are characteristic for FeS clusters. Colorimetric analyses revealed 0.48 ± 0.14 iron and 0.45 ± 0.12 sulfides per hTrx1 monomer after purification. The freshly purified protein was also subjected to gelfiltration chromatography, where it separated into a monomeric and a dimeric fraction (Fig. 1A inset, Fig. S1, †Supplementary Informations). From these, only the dimeric fraction (27.71 kDa, theoretical MW of hTrx1 dimer: 27.89 kDa) displayed the additional absorption features, whereas the monomeric fraction (13.95 kDa, theoretical MW of Trx1 monomer: 13.90 kDa) was completely devoid of them (Fig. 1A). Reduction of the recombinant holo-proteins by DTT led to the loss of all spectral features characteristic for FeS clusters.

An ideal method for the identification and characterization of iron centers is Mössbauer spectroscopy. Hence, apo-human Trx1 was subjected to FeS cluster reconstitution for the enrichment of the holo complexes with ^{57}Fe. Mössbauer spectra were recorded for holo-Trx1 at 77 K (Fig. 1B) and at 4.6 K in external magnetic fields (Fig. S2A-B). The spectra were simulated with two components (fractions 1 and 2) with a relative contribution of ca. 20 % and 80 %, respectively (Fig. 1B, Fig. S2A-B, Tab. 1, Tab. S1). Fraction 1 shows an isomer shift of $\delta = 0.35$ mm s^{-1} and a quadrupole splitting of $\Delta E_Q = 0.66$ mm s^{-1}. δ is slightly higher than the values reported for high spin Fe^{3+} (S = 5/2) in a tetrahedral sulfur environment ($\delta = 0.20 - 0.32$ mm s^{-1}) (22). It is important to note that both δ and ΔE_Q are significantly smaller than those reported for [4Fe-4S]$^{2+}$ clusters (23). The simulations of the spectra recorded in an external field of 0.1 T (Fig. S2A) and 5 T (Fig. S2B) are based on a

diamagnetic species for fraction 1. Hence we conclude that this fraction represents a diamagnetic $[2Fe\text{-}2S]^{2+}$ cluster in which the antiferromagnetic coupling of the two paramagnetic Fe^{3+} ions results in an S = 0 state (22–24). Fraction 2 is characterized by $\delta = 0.56$ mm s^{-1} and $\Delta E_Q = 0.72$ mm s^{-1}. These Mössbauer parameters are characteristic for high spin Fe^{3+} with octahedral nitrogen or oxygen coordination. The broad magnetic pattern observed at 4.6 K and fields of 0.1 and 5 T indicate the presence of small super-paramagnetic clusters that could originate from side reactions during the reconstitution process, possibly also from the decomposition of $[2Fe\text{-}2S]^{2+}$ clusters (25, 26).

The Mössbauer spectra of fraction 1 demonstrate the presence of $[2Fe\text{-}2S]^{2+}$ clusters in dimeric holo-Trx1. Reconstitution of the FeS cluster in apo-Trx1 revealed approximately 30 ± 14 % holo-Trx1 (Mössbauer and UV-Vis spectroscopy), 40 ± 16 % of Trx1 were in the holo-form directly after purification from *E. coli* (UV-Vis spectroscopy). To identify the residues responsible for the coordination of the cluster, we individually mutated each of the five Cys residues of human Trx1 to Ser. To exclude that a loss of cluster ligation in any of the mutants was caused by structural instability of the proteins, we confirmed their thermal stability by differential scanning calorimetry or fluorimetry (Fig. S3A, Tab. S2). Only the loss of one of two Cys residues led to the loss of the cluster binding, *i.e.* the more N-terminal active site residue C32 and the extra C73 outside the active site (Fig. 1C). Mouse Trx1 contains an additional C46, however, a C46S mutant was still able to coordinate the FeS cluster (Fig. 1C).

Can a $[2Fe\text{-}2S]^{2+}$ cluster be complexed at the dimeric interface of two Trx molecules by a pair of C32/C73 ligands as simulated in Fig. 1D? In various structures of human Trx1 deposited in the protein data bank, the sulfur groups of these two residues are separated by a distance of approx. 10 Å (Fig. S4A). This distance is too far for the joint coordination of the cofactor. However, as demonstrated by molecular modeling, only a small conformational change of the loop connecting helix 3 and strand 4 may bring the two sulfur atoms in a perfect distance for the coordination of the cluster, *i.e.* 3.4 Å (Fig. S4A). The

molecular dynamics (MD) simulations of the proposed model show no significant change of the overall secondary structure after the first 100 ns of the simulation (Fig.1E), thus, suggesting the stability of the proposed model. A small conformational difference between holo- and apo-Trx1 was confirmed by CD spectroscopy (Fig. 1F). These changes are proposed to go along with conformational changes of the two W31 residues (Fig. 1D), that should alter the local environment of the indole ring systems. In fact, formation of the holo complexes induces quenching of the fluorescence of these (only) tryptophanyl residues (Fig. 1G). The solvatochromatic nature of the Trp residues makes it sensitive to changes in the polarity of the local environment (27). Quenching can arise both from changes in the interaction with the solvent water molecules as well as altered interactions with other side chains in the complex. The conformational changes of the loop structure proposed to accommodate [FeS] binding also affect the orientation of lysyl residue K72. Our model suggests that the dimeric holo complex may be stabilized by a direct interaction between the ε-amino groups of the K72 residues with the carboxyl groups of S90 of the respective other subunit (Fig. 1D). In line with this hypothesis, Trx1K72E lost the spectral characteristics of the $[2Fe\text{-}2S]^{2+}$ cluster coordinated by wt Trx1 (Fig. S4B) and is less stable (Fig. S3B, Tab. S2). However, the redox activity was only affected to a minor degree since the mutated form was still able to reduce insulin disulfides and can be reduced by TrxR1. The K_m of TrxR1 towards Trx1K72E increased from 3.0 ± 0.2 to 4.4 ± 1.7 $\mu mol \cdot l^{-1}$, the v_{max} slightly increased from 2.7 ± 0.1 to 3.1 ± 0.5 s^{-1} (Fig. S4C). The decreased affinity of TrxR for Trx1K72E was likely the result of changes in the electrostatic properties of the mutant (Fig. S4D-E). In addition to K72, several other amino acids might contribute to the stabilization of the dimer (Fig. S4F). All these data confirm the formation of a holo-dimer using cysteinyl residues C32 and C73 as FeS cluster ligands. C73 is neither present in the mammalian mitochondrial Trx2, nor in bacterial Trxs, and none of these proteins contain a chromophore (Fig. S5).

Does human Trx1 bind the iron cofactor also *in vivo* as suggested by incorporation of the FeS clusters into Trx1 during recombinant expression in *E. coli* (Fig. 1A)? To answer this question, we propagated Jurkat cells of human origin in the presence of transferrin-bound radioactive ^{55}Fe. Trx1 and, as control, glutaredoxin (Grx) 1 that does not bind iron (28, 29), were immuno-precipitated from the cell extract and analyzed by scintillation counting for iron binding. Significant amounts of iron co-precipitated with Trx1, but not with Grx1 (Fig. 2A).

Trx1 and cellular iron metabolism

Since FeS cluster coordination blocks the CxxC active site, we assumed a Trx1-dependent connection between redox and iron regulation. Using Trx1C35S, a mutant lacking the second resolving cysteinyl residue of the active site, we were able to trap and identify potential substrates of Trx1 in HeLa cells (Fig. 2B). IRP1, the post-transcriptional iron regulator located in the cytosol of mammalian cells, was one of these substrates (Fig. 2C and 2D). In addition, Trx1 was confirmed as interaction partner of IRP1 using co-immunoprecipitation under untreated and H_2O_2 treated conditions in Jurkat cells (Fig. 2E). Based on this, we analyzed the consequence of Trx1 depletion on the level of IRP1-regulated proteins. Since IRP1 is also an important regulator of hypoxia response, HeLa cells were cultivated at 1% oxygen to inhibit the proteasomal degradation of HIF2α and treated with the iron-chelator deferoxamine (DFO), thus provoking both iron-depletion and hypoxia responses. Using specific siRNA, Trx1 levels were lowered to less than 10 % (Fig. 2F). Effective iron depletion was shown by significant lower levels of phosphoribosylpyrophosphate amidotransferase (PPAT) (Fig. 2F), a metabolic enzyme that is degraded when incorporation of its FeS cluster fails. However, depletion of Trx1 had no relevant effect on the diminished cytosolic FeS cluster biogenesis. Cellular amount of IRP1 itself was almost not affected (Fig. 2F). It was slightly lower in iron-depleted cells and under all tested condition a bit higher in Trx1 lacking cells (132 ± 9 %). The HIF2α

encoding mRNA, one of the main targets of IRP1, contains an IRE in its 5´ region. Hence, translation of HIF2α is blocked by IRP1 binding. This block is not present in cells lacking Trx1 (Fig. 2F). In these cells, the HIF2α levels increased up to 231 ± 49 % and 342 ± 57 % if iron was absent. Surprisingly, levels of the iron storage protein ferritin did not increase upon Trx1 deficiency (Fig. 2F), although the respective mRNA contains an IRE in its 5` region as well.

Human Trx1 reduces Iron-Regulatory Protein 1 in vitro *and* in vivo

Next, we tested recombinant oxidized human apo-IRP1 as substrate for Trx1 in a coupled assay with TrxR1 following NADPH consumption. As depicted in Fig. 3A, apo-Trx1 was able to reduce and thus activate IRP1 *in vitro* with a K_m of 18.5 µM and a v_{max} of 0.41 s^{-1}. To confirm that only apo-IRP1 is a substrate, we performed the above described assay in an anaerobic chamber using purified holo-IRP1 with and without cluster removal. With 16 µM apo-IRP1 we measured an enzymatic Trx1 activity of 5.94 ± 2.82 µM/min and with holo-IRP1 3.12 ± 2.4 µM/min (Fig. 3B) indicating that apo-IRP1 is the main target for Trx1.

Does Trx1 also fulfill this function *in vivo*? We analyzed the redox state of IRP1 in Trx1-depleted HeLa cells compared to cells treated with control siRNA via two dimensional diagonal gel electrophoresis. In the first dimension, the proteins were separated by non-reducing SDS PAGE, the second dimension was SDS PAGE under reducing conditions. In this assay, reduced proteins end up on a diagonal according to their molecular weight (Fig. 3C-D). Proteins with oxidized cysteinyl residues, however, drop below the diagonal. As demonstrated by an overlay of Coomassie-stained gel and Western blot detecting IRP1, all IRP1 in control cells was in the reduced state (Fig. 3C). Upon Trx1-depletion, however, most of the IRP1 protein was oxidized (Fig. 3D). Apparently, Trx1 is required for the reduction, and thus activation, of IRP1 *in vivo*. Accordingly, lower levels of Trx1 led to increased aconitase (holo-IRP1) activity in the cytosol of hypoxic HeLa cells under iron depletion (Fig. S6), whereas the protein level of aconitase/IRP1 was not affected (Fig. 2F).

Trx1 regulates IRP1 binding to the Hif2α-IRE

The HIF2α mRNA has been demonstrated to be one of the major targets of IRP1 (18). It has long been known from *in vitro* assays that the binding of IRP1 to IREs requires the reduction of the cysteinyl residues in the IRE binding site, see *e.g.* (10). These residues are also the residues coordinating the FeS cluster within IRP1 that is lost upon iron depletion. These cysteinyl residues are prone to be oxidized once the cluster is gone. Therefore, we tested whether reduction of IRP1 by Trx1 affects IRE binding. Whereas Trx1 depletion via siRNA (Fig. S7A) showed no impact on IRP1/HIF2α-IRE binding in whole lysates of cells cultivated under standard conditions, the increased IRP1/HIF2α-IRE binding in wildtype cells under iron limited and hypoxic conditions (300 ± 36 % compared to untainted cells) was severely and significantly diminished in Trx1-depleted HeLa cell lysates (only 160 ± 17 %) in electrophoretic mobility shift assays (EMSAs, Fig. 3E). The diminished IRE binding capacity was slightly more pronounced in the purified cytosolic fraction (48 ± 15 %, Fig. S7B) compared to the whole lysate (57 ± 7 %, Fig. 3E). Moreover, decreased IRE binding upon Trx1 depletion was determined in EMSAs under hypoxic or iron depleting conditions alone in whole lysate (Fig. 3E) and even under standard conditions in the isolated cytosolic fraction (Fig. S7B). As shown before (Fig. 2F), the lack of Trx1 does not affect IRP1 levels and reduction of lysates with DTT further showed that decreased IRP1/HIF2α-IRE binding upon Trx1 depletion is not based on decreased levels of IRP1. Indeed, the formation of IRP-IRE complexes increased in lysates of control cells after incubation with DTT only to 115 ± 16 %, but to 194 ± 56 % in lysates of Trx1 lacking cells reaching 72 ± 8 % of complex formation in DTT-treated lysates of control cells (Fig. S7C). Formation of supershift complexes after addition of anti-IRP1-antibodies confirmed IRP1-IRE probe complexes (Fig. S7D and S7E). EMSAs with purified recombinant IRP1 and Trx1 demonstrated direct reduction and activation of IRP1 by Trx1. 10 µM of Trx1 is as efficient as 10 mM β-mercaptoethanol in the activation of 1 µM IRP1 (Fig. S7E). IRE binding increased to 359 ± 92 % in presence of apo-Trx1 and to 251 ± 51 % in presence of

β-mercaptoethanol. The blocking of the CxxC active site by coordination of the FeS cluster after reconstitution diminished the ability of Trx1 to activate IRP1 to 44 ± 12 %, whereas incubation with Fe^{2+} most likely leading to unspecific iron binding had no effect on Trx1 activity in modulating IRP1/HIF2α-IRE binding (97 ± 4 %, Fig. 3F). IRP1 contains nine cysteines. The three cysteinyl residues essential for both FeS cluster coordination in holo-IRP1 and IRE binding in apo-IRP1 are C437, C503, and C506 (Fig. 3G). These cysteines are close together in the holo-form (approximately 6 Å), but shift 18.2, 22.8, and 27.4 Å, respectively, to their positions in the apo-form where the distance between C437 and C503 or C506 is 12.5 and 17 Å (Fig. 3H). Based on the electrostatic surface potential maps of apo-IRP1 and apo-Trx1, we predict that the active site of Trx1 most likely attacks either C503 or C506 (Fig. 3I). Therefore, we hypothesize the formation of a disulfide in IRP1 between cysteinyl residues 437 and 503/506 after disassembly of the FeS cluster that inhibits IRE binding and the need for active Trx1 to reduce this disulfide and to rescue the IRE binding activity of apo-IRP1.

Discussion

In the present study, we characterized the human and murine cytosolic Trx1 as new FeS-proteins. The $[2Fe\text{-}2S]^{2+}$ cluster is coordinated at the dimeric interface of two Trx molecules. Approximately a decade ago, we have characterized human Grx2 as the first member of the Trx family that contains an FeS cofactor (29). The $[2Fe\text{-}2S]^{2+}$ cluster in Grx2 is coordinated by the N-terminal active site Cys of two monomers plus two additional non-covalently bound glutathione molecules (30, 31). Because the glutathione used as FeS ligand is in permanent exchange with the free pool of glutathione, the iron complex was described as a redox sensor that could regulate the oxidoreductase activity depending on the redox state of the free glutathione pool (30). Holo-Grx2 is inactive as oxidoreductase, but appears to be involved in nitric oxide detoxification during neuroinflammation (32). Enzymatically active apo-Grx2 is required, for instance, for brain and vascular development (33, 34), and promotes cell migration of cancer cells (35, 36). The same mode of cluster coordination was also demonstrated for the human monothiol Grxs 3 and 5 (28, 37) that function in iron homeostasis and FeS cluster biosynthesis, as well as for various Grxs from other species, for overviews see for instance (38, 39). Fig. 4A depicts the overlay of the iron-coordinating thiol groups in human Trx1, Grx2, and Grx5, centered on the common N-terminal active site cysteinyl residue (C32 in Trx1) indicating that FeS cluster coordination by Trx family proteins needs a second thiol group in the suitable distance range to the active site thiol. Whereas Grxs insert this thiol via the bound glutathione, human Trx1 uses as second thiol the side-chain of the not universally conserved C73. The position of this second thiol appears to be variable, due to the dimeric nature of the holo-complexes. The slightly shifted positions of the glutathione thiols and FeS centers are caused by alternative loop structures preceding the active sites. These differences are also the structural basis for the functional difference (oxidoreductases or FeS cluster transferases) between the two classes of vertebrate glutaredoxins (40). The different positions of the glutathione thiol cause a rotation of the two Grx monomers in the

Grx2 and Grx5 holo-complexes relative to each other (31, 37). Likely, this is also true for the Trx1 holo-complex, although Mössbauer spectroscopy revealed a slightly higher value of δ than found usually for [2Fe-2S] clusters coordinated by four sulfhydryl groups. This increase could be related to the presence of a nitrogen or an oxygen ligand (22, 24). Recently, for the bishistidinyl-coordinated non-Rieske $[2Fe\text{-}2S]^{2+}$ proteins a value of δ = 0.36 mm s^{-1} has been reported for the bis-histidyl coordinated Fe^{3+} site at pH=6 (41). However, the only nitrogen or oxygen available for cluster coordination near the active site would be the histidyl residues introduced by the His-tag. Since we used both, C- as well as N-terminal His-tags, and were able to show that specific Trx1 mutants affect cluster coordination independent on the His-tag, we are confident that the cofactor is coordinated by cysteinyl residues 32 and 73. In retrospect, this coordination was already indicated by our own work showing that only the additional removal of these two cysteinyl residues in human Trx1 inhibited [2Fe-2S] cluster coordination in a mutant lacking the *cis*-proline (P75 in human Trx1), another feature regulating FeS cluster coordination in members of the Trx family (42). However, recently a [4Fe-4S] cluster coordinated by the residues of the two active side cysteinyl residues was described in *A. thaliana* Trx o (43). This Trx is located in mitochondria, contains a *cis*-prolyl residue, and lacks the additional C73 which serves as second thiol in a similar position as in the FeS-Grxs. In addition, some Trx-type/Trx-related proteins were identified as FeS proteins, *e.g.* dimers of *E. granulosus* iron-sulfur Trx-related protein (IsTRP) and *T. brucei* Trx2 coordinate [2Fe 2S] clusters (44, 45). Several mutants of *E. coli* Trx with engineered active site sequences are able to coordinate [2Fe-2S] clusters as well (46, 47). In general, the Trx fold seems to be well suited for the coordination of metal cofactors as shown by many other engineered and wildtype proteins (48). C73 is not an ubiquitously conserved residue. We have performed an extensive sequence comparison between Trxs from various species, classes, and kingdoms, see Fig. S8. This analysis identified the extra C73 as specific for vertebrate cytosolic Trxs, with only few exceptions in arachnid species and one mollusk. C73 is not present in Trxs from

bacteria, fungi, plants, insects, nematodes, or mitochondrial vertebrate Trxs. We have expressed and purified both *E. coli* Trx1 and human mitochondrial Trx2 in the same way as human and mouse Trx1 and did not detect any signs for cluster binding (Fig. S5). Hence, nearly all potential FeS-Trxs exist in the same evolutionary group that utilize the IRP/IRE system for the regulation of iron-uptake and storage (also included in Fig. S8); all of the C73-Trxs are cytosolic proteins. Only one previous study linked Trx1 to the IRP regulon. In macrophages, Trx1 was reported to be required for the activation of IRP1 after exposure to nitric oxide (11). Trx1 is able to reduce IRP1 *in vitro* and *in vivo* leading to increased IRE binding of HIF2α mRNA (Fig. 3). The importance of the reduction of the cysteinyl residues in the FeS cluster coordination site of IRP1, that is also the IRE binding site, has long been known from *in vitro* assays *e.g.* (10). Here, we focus on the redox state of cysteinyl residues. However, also other amino acids may contribute to the redox regulation of IRP1 activity, *i.e.* tyrosine nitration by peroxynitrite (49). When iron is not limiting, IRP1 (gene name ACO1) is a functional cytosolic aconitase with a [4Fe-4S] cluster in its active site that is ligated by three cysteinyl residues. This cluster is lost when iron becomes a limiting factor, IRP1 undergoes structural changes between holo- and apo-form, and the resulting apo-protein can bind IRE stem loop structures in mRNAs (Fig. 3G). The three cysteinyl residues C437, C503, and C506 bind either the FeS cluster or the IRE. The redox state of C437 has been described before as important for IRE binding (51). Only mutation of this cysteinyl residue rescued the lost IRP1-IRE binding upon treatment with either N-ethyl-maleimide, a molecule blocking free thiols, or diamide, a compound that unspecifically induces the formation of disulfides. Of course, formation of a disulfide needs two cysteinyl residues. The interaction between Trx and a substrate critically depends on complementary electrostatic properties (52, 53). Based on these properties, Trx1 might reduce a disulfide between cysteinyl residues 437 and 503/506 (Fig. 3I). The formation of a disulfide that may prevent IRE-binding was suggested before (54). This is, however, in contrast to several reports describing the activation of IRP1 by H_2O_2, summarized in (55).

Noteworthy, this activation can be observed only at low concentrations of H_2O_2 in cells and not in lysates. In intact cells, low levels of H_2O_2 most likely activate the Keap1/Nrf2 system, which leads to the expression of various enzymes counteracting oxidative damage, including Trx1, that subsequently promote the activation of IRP1. In line, recombinant holo-IRP1 lost its FeS cluster upon H_2O_2 treatment but did not gain IRE binding capacity (57).

Lack of Trx1 led to a massive increase in HIF2α, despite conditions of iron-limitation, while ferritin was hardly affected (Fig. 2F). That was not expected as both RNAs contain the IRE at the 5´ region. However, as described before (57), hypoxia-dependent increase of ferritin levels seem to be cell specific. Moreover, ferritin iron-loading in the experiments of Fig. 2F may be different. Last, hypoxic and iron-scavenging kinetics might differ. In case of cellular response to hypoxic conditions, a redox-dependent signaling element would be useful. A comparison between the IREs of ferritin and HIF2α reveales two guanine bases that are absent in the IRE of ferritin. These guanine bases are located between C8 and the conserved CAGUG motif in the top of the IREs, the two areas forming the majority of bonds with IRP1 (58). Since guanine exist as oxidized base changing RNA binding specifity (59) we do not want to exclude another level of regulation, *e.g.* IRE oxidation (49). Mammalian IRP1 and IRP2 share functions (61), but are differently affected by hypoxia: IRP1 is inhibited, while IRP2 is activated (62, 63), although data that suggest the activation of IRP1 during hypoxia have also been presented (57, 64). Several studies, including analyses of knock-out mice, emphasized the pivotal function of IRP1 in the suppression of HIF2α translation under iron limiting conditions (16–18). HIF2α is an essential regulator of erythropoiesis and angiogenesis, as well as cell proliferation, de-differentiation, and invasion of cancer cells via its various target proteins (18, 20, 21, 65).

HIF2α is primarily regulated by suppression of its translation through IRP1 under iron-limiting conditions and the O_2-dependent proteasomal degradation pathway. This study adds a third level of regulation to the IRP1-HIF2α signaling hub, *i.e.* redox regulation. The

lack of Trx1 activity in cells leads to the loss of HIF2α suppression even under iron-limiting conditions. Fig. 4B summarizes this extended model of IRP1 activation and thus permission or suppression of HIF2α translation. Activation of both Trx1 and IRP1 requires conditions that lead to the loss of their iron-sulfur cofactors (Fig. 3E). Next, activation of IRP1 requires the reduction of the protein by Trx1 with electrons donated by TrxR1 and NADPH. Limitation of the reducing power of the Trx system may explain the limited ability of IRP to regulate exogenous IREs in transfected cellular systems (66). Only when both conditions are met, iron limitation and sufficient reducing power of the cytosolic Trx system, IRP1 can bind to the IRE in the 5'-end of the HIF2α mRNA and thus suppresses its translation and accumulation of the transcription factor under hypoxic conditions. In support of this model, all mentioned HIF2α processes are also redox-regulated on multiple levels, many of which are dependent on Trx1, summarized in (4).

Methods

Cloning, protein expression and purification:

Human and mouse Trx1 were cloned into the expression plasmids pet20b and pet15b as described before (42, 67). Mutations were inserted by rolling circle mutagenesis using specific oligonucleotides (C32S: fwd: cagccacgtggtctgggccttg, rev: caaggcccagaccacgtggctg; C35S: fwd: tggtgtgggccttccaaaatgatc, rev: gatcattttggaaggcccacacca; C62S: fwd: gtggatgactctcaggatgttgc, rev: gcaacatcctgagagtcatccac; C69S: fwd: gttgcttcagagtctgaagtcaaatg, rev: catttgacttcagactctgaagcaac; C73S: fwd: gaagtcaaatccatgccaacattcc, rev: ggaatgttggcatggatttgacttc; K72E: fwd: tcagagtgtgaagtcgagtgcatgccaacattc, rev: gaatgttggcatgcactcgacttcacactctga). IRP1 was cloned by PCR from human cDNA using specific oligonucleotides (fwd: gctagcatgagcaacccattcgcac, rev: ctcgagcttggccatcttgcggatcatg), digested with NheI and XhoI, and cloned into the vector pET16b (Novagen). Proteins were produced in *E. coli* as His-tag proteins and were purified using the IMAC principle (GE healthcare). Following purification, proteins were buffered in PBS using NAP-5 columns (GE healthcare) or Zeba spin columns (Thermo Scientific). The thermal stability of Trx1 mutated forms was analyzed using differential scanning calorimetry or fuorimetry. 10 or 40 µM of the proteins in PBS were heated from 20 to 100 °C at 0.2 - 1 K per minute in a Micro Cal VP-DSC (Malvern Panalytical Ltd) and the heat flux was recorded or, for DSF, followed in a BioRad CFX qPCR instrument. The melting point (T_m) of DSF was identified by fitting the melting curve with Boltzmann equation (eq.1). In this equation FU is the measured fluorescence signal from Sypro Orange.

$$FU = a_1 + \frac{a_1 - a_0}{1 + exp(fracT_m - Ts)} \qquad \text{(eq.1)}$$

Gelfiltration chromatography for the separation of monomeric and dimeric Trx1 was performed as outlined in (28).

In vitro reconstitution

Reconstitution of the FeS cluster was performed as described in (30) without GSH. For Mössbauer spectroscopy apo-Trx1 was reconstituted using $(NH_4)_2{}^{57}Fe(SO_4)_2$ as iron source.

Spectroscopy

Following purification, reconstitution, and buffering in PBS, proteins were desalted using NAP-5 columns, UV-Vis spectra were recorded using 100-250 µM of wildtype and mutant proteins with the Uvikon 922 photometer (Kontron Instruments) from 240-720 nm. Circular dichroism (CD) spectra were recorded with 10 µM apo- and holo-Trx1 in a 1 mm cuvette, scanning 0.2 nm steps, averaging 5 iterations, with the Jasco J-810 instrument. Tryptophanyl fluorescence was recorded with a Perkin Elmer LS50B fluoriometer (10 $\mu mol \cdot l^{-1}$ protein, excitation: 296 nm, 6 nm excitation slit and 4 nm emission slit).

A conventional Mössbauer spectrometer was operated in the constant acceleration mode in conjunction with a multichannel analyzer in the time-scale mode (WissEl GmbH) to record transmission Mössbauer spectra. The spectrometer was calibrated against α-iron at room temperature. The samples were cooled to 77 K with a flow cryostat (OptistatDN, Oxford Instruments). Field-dependent conventional Mössbauer spectra were obtained with a helium closed-cycle cryostat (CRYO Industries of America, Inc.) equipped with a superconducting magnet (68). The magnetic field direction parallel to the γ-ray beam. The spectral data were transferred from a multichannel analyzer to a PC for further analysis employing the public domain program Vinda (69) running on an Excel (2003) platform. Analysis of the spectra was performed by least-squares fits using Lorentzian line shapes with the linewidth Γ. Field-dependent spectra were simulated by means of the spin Hamilton formalism (70). Following *in vitro* reconstitution, human Trx1 was concentrated to 2.5 mM using the Stirred Ultrafiltration Cell (Millipore) and buffered in PBS using PD-10 columns (GE Healthcare). $(NH_4)_2{}^{57}Fe(SO_4)_2 \cdot 6H_2O$ was synthesized in a procedure

adapted from (71). In brief, 102.9 mg (1.768 mmol, 1 eq) of ^{57}Fe were dissolved in 2.6 ml of 1 molar sulfuric acid with continuous heating under N_2 atmosphere. The resulting turquoise solution was filtered from the deposited coke. To this solution, 243.14 mg (1.84 mmol, 1 eq) ammonium sulfate in aqueous solution were added. Next, the solution was concentrated under reduced pressure and allowed to form a crystalline surface; the concentrated solution was heated and stored by 4 °C to allow crystallization. The resulting turquoise crystals were collected and the procedure was repeated for the remaining solution. In the end, 67.7 % of the initial iron was present as highly pure $(NH_4)_2{}^{57}Fe(SO_4)_2 \cdot 6H_2O$ crystals, as confirmed by X-ray analysis (72).

Activity measurements

The activity of cytosolic aconitase was determined as described in (73). The activity of Trx1 in the reduction of IRP1 was measured in a coupled optical assay with rat thioredoxin reductase and NADPH as outlined in (74). The reduction of insulin in a coupled assay of Trx with TrxR has been performed following the reduction of NADPH spectrophotometrically. The assay mixture contained 50 mmol·l^{-1} Tris/HCl pH 7.5, 2 mmol·l^{-1} EDTA, 160 µmol·l^{-1} insulin (SIGMA-Aldrich), 150 µmol·l^{-1} NADPH, 1.25 nmol·l^{-1} recombinant rat TrxR1 (kind gift from Elias Arner, Stockholm), and Trx from 0 – 25 µmol·l^{-1}. Holo-IRP1 used as substrate was purified under anaerobic conditions as described in (56). The FeS cluster was removed according to (50) by incubation of the protein with 200 µM H_2O_2 and 10 mM EDTA for 1 h at room temperature following filtration through a Zeba spin column (Thermo Scientific). The respective activity assays were performed in an anaerobic chamber (Coy Laboratory Products, USA).

Cell culture

HeLa cells were cultured in low glucose (1g/l) DMEM medium, supplemented with 10 % FCS and 100 units/ml penicillin 0.1 mg/ml streptomycin at 37 °C in a humidified atmosphere containing 5 % CO_2. Cells were transfected with specific siRNA against

human Trx1 by electroporation. $3.5 \cdot 10^6$ cells were resuspended in electroporation buffer (21 mM HEPES, 137 mM NaCl, 5 mM KCl, 0.7 mM Na_2HPO_4, 6 mM D-glucose, pH 7.15), were mixed with 15 µg of Trx1 siRNA (sense: guagauguggaugacuguc, antisense: gacagucauccacaucuac) or scrambled control siRNA (sense: cauucacucaggucauca, antisense: cugaugaccugagugaau) and were electroporated at 250 V, 1500 µF and 500 Ω using the BTX ECM 630. FCS was immediately added to the cells before seeding them in 1:5 conditioned medium. The following day the medium was changed. For sufficient knock-down, cells were transfected a second time after three days and cultivated for another 2 days at 20 % oxygen followed by 24 h at 1% oxygen concentration. To reduce intracellular iron levels, cells were treated for 24 h with 100 µM deferoxamine (Abcam). Cells were harvested by trypsination, incubated with PBS containing 100 mM NEM for 5 min at RT. Cells were centrifuged and washed once in PBS, before 30 min lysis in 40 mM HEPES, 50 mM NaCl, 1 mM EDTA, 1 mM EGTA, 2 % CHAPS, complete protease inhibitor, and 100 mM NEM. Samples were stored at -80 °C. The knock-down efficiency, as well as the iron depletion was analyzed by Western blot using specific antibodies against Trx1 and iron-regulated proteins.

Jurkat cells were cultured in RPMI medium supplemented with 10 % FCS, 100 units/ml penicillin and streptomycin, and 2 mM glutamine at 37 °C in a humidified atmosphere containing 5 % CO_2. Radiolabeling was done with 1 mCi, 2 µM transferrin-^{55}Fe (Perkin-Elmer). Co-immunoprecipitation of ^{55}Fe with Trx1 and Grx1 was performed as described for Grx3 in (28).

Cell fractionation was performed according to (73). Cells were resuspended in mitobuffer (5 mM Tris/HCl, 250 mM Sucrose, 1 mM EDTA, 1 mM EGTA, 1.5 mM MgCl2, 1 mM PMSF, pH 7.4), containing 0.008 % digitonin, and were incubated for 10 min on ice. Cells were centrifuged for 10 min at 15.000 g at 4 °C. The supernatant was collected as cytosolic fraction. The pellet was washed 2 times, resuspended in mitobuffer, and collected as organelle-fraction.

Electrophoresis, Electrophoretic mobility shift assay, and Western blotting

Cell lysates were thawn on ice and centrifuged at 4 °C for 15 min at 13.000 rpm. The protein content of the supernatants was analyzed according to Bradford (BioRad). 20-30 µg of total protein were diluted in sample buffer (5-fold: 0.3 M Tris/HCl, pH 7, 50 % glycerol, 5 % SDS, 10 mM EDTA, 0.1% bromphenol blue), were reduced with 100 mM DTT for 20 min at RT. Proteins were separated by SDS PAGE using Mini-Protean TGX stain-free 4-20 % precast gels (BioRad).

For the electrophoretic mobility shift assay (EMSA), we synthesized IRD700 labeled RNA used as Hif2α-IRE sequence before GGCUCCUGAGGCGGCCGUACAAUCCUCGGCAGUGUCCUGAGACUGUAUGGUCAG CUCAGCCCAUG (16) (Metabion, Germany). According to manufacturer and Anderson et al. (16), the IRE was folded in 60 mM KCl, 6 mM HEPES, 0.2 mM $MgCl_2$ via heating to 90°C for 2 minutes and cooling on ice for 5 min. 2 µl of 0.1 µM RNA was mixed with 20 µg cell lysate or 1 µM recombinant IRP1 and 10 µM recombinant Trx1 or 300 mM DTT or 10 mM β-mercaptoethanol in 20 mM HEPES pH 7.4. Samples were incubated with 20 µg/ml BSA for 10 minutes at RT followed by addition of heparin to 0.5 µg/µl. For supershift, 1 µl of 1:20 diluted selfmade α-IRP1-antibodies (75) was added for another 2 minutes. SDS PAGE was run as native gel (native PAGE buffer: 25 mM Tris, 192 mM Glycine, pH 8.3) at 120 V in the dark. Afterwards the probe was detected at 700 nm using Odyssey Infrared Imaging System (LI-COR Bioscience).

The 2D diagonal redox SDS PAGE was performed modifying the protocol described by (76). In brief, 40 µg cell lysate was mixed with sample buffer, denatured for 10 min at 96°C before it was separated at a 4-20 % PROTEAN TGX stain-free gel (BioRad) at 200 V for 30 min. The protein lane was cut out and reduced in 250 mM DTT in 1-fold sample buffer at 65 °C. The gel was washed in 1-fold sample buffer, before the proteins were alkylated for 20 min at a reciprocal shaker using 100 mM NEM in 1-fold sample buffer. The gel was

washed in 1-fold sample buffer again before it was placed at a 4-20 % PROTEAN TGX IPG gel. A molecular weight marker was added and the gel lane was overlaid with 1% agarose in 1-fold sample buffer. The proteins were separated at 50 V for 10 min, followed by 200 V for 30 min.

The protein content of all gels (and later the blots) was imaged after activation using BioRads stain-free technology with the ChemiDoc XRS+ System. Western blotting was performed using the Trans-Blot Turbo RTA Transfer Kit (BioRad), according to the manufacturers protocol using PVDF membranes. Membranes were blocked with Tris-buffered saline containing 0.05 % Tween 20, 5% nonfat milk powder and 1 % BSA for 1 h at RT and were incubated with specific primary antibodies against Trx1 (67), PPAT (kindly supplied by R. Lill, Marburg Germany), IRP1 (abcam ab126595 for 1D gels and for 2D gels see reference (75), ferritin (abcam ab75973), and the transferrin receptor (Life technologies 13-6890) at 4 °C overnight. Using horseradish peroxidase (HRP)-coupled secondary antibodies (BioRad) and the enhanced chemiluminescence method antigen–antibody complexes were detected by the ChemiDoc XRS+ System (BioRad). The densitometric analysis was performed using ImageJ and the ImageLab 5.0 Software (BioRad).

Identification of interaction partners

Co-immunoprecipitation of IRP1 and Trx1 was performed using CnBr activated sepharose. 100 mg sepharose beads were incubated with IRP1 antibodies (28) corresponding to the equivalent of 1 ml serum. After washing steps with PBS, the sepharose beads were blocked with 1 M ethanol amine. 20 µl antibody conjugated sepharose beads were incubated with 1 mg protein lysate at 4 °C over night. After removing unbound proteins, the sepharose and bound proteins were denatured for 10 min at 95 °C and Trx1 was stained after performing a reducing SDS PAGE and Western blotting.

The intermediate trapping was performed by immobilizing Trx1C35S on a HisTrap column. Following reduction with 10 mM DTT, 10-20 mg HeLa cell lysate were loaded on the column. Following extensive washing, trapped proteins were eluted with 10 mM DTT, were precipitated over night at 4 °C with 20 % TCA and were centrifuged for 15 min at 13.000 rpm and 4 °C. The pellet was washed with ice cold acetone, centrifuged again and resuspended in lysis buffer. The presence of IRP1 was analyzed by SDS-Page and Western Blotting using the IRP1 antibody described in (28) and mass spectrometry. Samples were prepared for mass spectrometric analysis by in-gel reduction, alkylation and digestion essentially as described earlier (77). Digested peptides were extracted from the gel, dried and resuspended in 0.1 % trifluoroacetic acid. Peptide samples were subjected to liquid chromatography (Ultimate 3000 rapid separation liquid chromatography system, Thermo Fisher Scientific) coupled tandem mass spectrometry (QExactive plus, Thermo Fisher scientific) as described in (77). Briefly, after a 2h separation of peptides on C18 material, separated peptides were injected via a nano-electrospray source into the mass spectrometer operated in positive, data-dependent mode. First, precursor spectra were recorded at a resolution of 140.000 followed by the quadrupole enabled isolation of up to ten precursors which were subsequently fragmentation by higher-energy C-trap dissociation and resulting spectra recorded at a resolution of 17.500. Peptide and protein identification was carried out with MaxQuant (version 1.6.17.0) on the basis of 75.777 homo sapiens entries (UniProt KB proteome, UP000005640, downloaded on 20210127). The “match between runs”, label-free quantification and iBAQ option were enabled, other parameters were not changed according to the standard settings.

Molecular modeling and Molecular Dynamics simulation

The suggested conformational changes required for the binding of the FeS cofactor to human Trx1 were modeled using SPDBV (78, 79). Based on the structure of reduced human Trx1 (pdb entry 1ert), we scanned the loop database for potential alternative conformations of the loop connecting alpha helix 3 and strand 4 of the central beta-sheet.

Glu70 and the *cis*-Pro75 were used as anchoring residues. The best fit was obtained with a model loop obtained from structure 2nacA (residues 25-28). The resulting structure was relaxed by energy minimization. The integrity and quality of the structure was confirmed using ProSA-web (80), the z-score of -6.9 was within the range of scores typically found for native proteins of this size. The proposed holo-structure of dimeric Trx1 was modeled based on the holo-structures of human Grx2 (2ht9) and human Grx5 (2wul), electrostactic calculations were performed as described in (53). Apo-IRP1, *i.e.* the missing loop containing cysteinyl residues 503 and 506, was modeled using Swiss Model (https://swissmodel.expasy.org/) with pdb entry 3sn2 as template. Structures were displayed using UCSF Chimera (https://www.cgl.ucsf.edu/chimera/).

Molecular Dynamics simulations were performed in Gromacs (Version 2021.3) (81)] with Amber99ff-ILDN force field (82) . The parameters for the [2Fe-2S] cluster coordinated from Carvalho *et al* (83) were used. The model protein was solvated with TI3P water in a cubic box under periodic boundary condition with 1 nm distance from the protein to the edge of the box. The simulation box was neutralised with Na^+ and Cl^+ ions.

Prior to the production simulations, the system underwent a three-step equilibration. The first energy minimisation was performed with steepest descent algorithm until the system converged to 1.000 kJ*mol-1*nm-1. The next equilibration step was performed with NVT ensemble with constant temperature of 300K for 100 ps, and the last step with NPT ensemble with constant pressure of 1bar and temperature of 300K. The time steps of 2 fs were used in the simulations. LINCS (84) algorithm was used for constrains of hydrogen bonding interactions. For pressure and temperature coupling the Parrinello-Rahman method (85) and modified Berendsen thermostat (86) were used, respectively. For the calculation of long-range electrostatic interactions the Particle Mesh Ewald (87) method was used, whereas for the short-range (both Coulomb and van-der-Waals) the Verlet cut-off scheme with 1.5 nm cutoff distance was used. The analysis of the simulations were

performed with Gromacs-intern tools, UCSF Chimera (88) was used for the graphical representation of protein structures.

Phylogenetic and statistical analysis

Sequences for Trx1 and IRP1/Aco1 were collected from the uniprot.org and pubmed databases. Alignments and the radial phylogenetic tree were created using the CLC Sequence Viewer 8. Alignments were used to analyze the presence of the active site Cys residues as well as the extra Cys73. Statistical significance was calculated using GraphPad Prism 5 (GraphPad Software) when $n \geq 4$ using Students t-test (*: $p<0.05$; **: $p<0.01$; ***: $p<0.001$).

Acknowledgements

The authors wish to thank C.A. Helm and A. Gröning (Greifswald) for help with the differential scanning calorimetry, Elias Arnér (Stockholm, Sweden) for providing mammalian TrxR, Ingrid Span (Düsseldorf/Erlangen, Germany) for help with the anaerobic chamber, and Rick Eisenstein (Madison, USA) for helpful discussions. This work was supported by grants from Plan Cancer (to JMM: n° 18CB010-00) and the Deutsche Forschungsgemeinschaft (DFG, German Research Foundation), in particular the Priority Program SPP 1927 (to CB: BE 3259/5-1,2, BE 3259/6-1, 417677437/GRK2578; to CHL: LI 984/3-1,2, LI 984/4-1, GRK1947-A1, to CSM: SCHU 1480/4-1, and to VS: SCHU 1251/17-1,2).

Author contributions

C.B., E.M.H., M.G., L.T., C.O.S., and C.H.L. performed biochemical and cellular experiments, E.M.H., S.S., Y.B., and O.H. cloned and purified Trx mutants, L.M.J., C.S.M., and V.S. performed Mössbauer spectroscopy, G.P. performed mass spectrometry, R.N. and C.S. synthesized and provided $(NH_4)_2{}^{57}Fe(SO_4)_2{\cdot}6H_2O$, Y.B. and C.H.L. performed bioinformatic analyses including MD simulations, J.M.M. provided critical input and material, C.B., E.M.H., and C.H.L. wrote the manuscript, all authors approved the text.

Declaration of Interests

The authors declare no competing interests.

References

1. C. H. Lillig, A. Holmgren, Thioredoxin and Related Molecules From Biology to Health and Disease. *Antioxid. Redox Signal.* **9**, 25–47 (2007).

2. T. C. Laurent, E. C. Moore, P. Reichard, Enzymatic synthesis of deoxyribonucleotides. iv. isolation and characterization of thioredoxin, the hydrogen donor from Escherichia coli B. *J. Biol. Chem.* **239**, 3436–44 (1964).

3. B. B. Buchanan, A. Holmgren, J.-P. Jacquot, R. Scheibe, Fifty years in the thioredoxin field and a bountiful harvest. *Biochim. Biophys. Acta* **1820**, 1822–1829 (2012).

4. E.-M. Hanschmann, J. R. Godoy, C. Berndt, C. Hudemann, C. H. Lillig, Thioredoxins, glutaredoxins, and peroxiredoxins--molecular mechanisms and health significance: from cofactors to antioxidants to redox signaling. *Antioxid. Redox Signal.* **19**, 1539–1605 (2013).

5. R. Lill, U. Mühlenhoff, Maturation of iron-sulfur proteins in eukaryotes: mechanisms, connected processes, and diseases. *Annu. Rev. Biochem.* **77**, 669–700 (2008).

6. H. Sies, C. Berndt, D. P. Jones, Oxidative Stress. *Annu. Rev. Biochem.* **86**, 715–748 (2017).

7. C. P. Anderson, M. Shen, R. S. Eisenstein, E. A. Leibold, Mammalian iron metabolism and its control by iron regulatory proteins. *Biochim Biophys Acta* **1823**, 1468–1483 (2012).

8. M. U. Muckenthaler, B. Galy, M. W. Hentze, Systemic iron homeostasis and the iron-responsive element/iron-regulatory protein (IRE/IRP) regulatory network. *Annu. Rev. Nutr.* **28**, 197–213 (2008).

9. M. L. Wallander, E. A. Leibold, R. S. Eisenstein, Molecular control of vertebrate iron homeostasis by iron regulatory proteins. *Biochim. Biophys. Acta* **1763**, 668–689 (2006).

10. O. Stehling, *et al.*, Investigation of iron-sulfur protein maturation in eukaryotes. *Methods Mol. Biol. Clifton NJ* **372**, 325–342 (2007).

11. L. Oliveira, C. Bouton, J. C. Drapier, Thioredoxin activation of iron regulatory proteins. Redox regulation of RNA binding after exposure to nitric oxide. *J. Biol. Chem.* **274**, 516–521 (1999).

12. A. A. Salahudeen, *et al.*, An E3 ligase possessing an iron-responsive hemerythrin domain is a regulator of iron homeostasis. *Science* **326**, 722–726 (2009).

13. A. A. Vashisht, *et al.*, Control of iron homeostasis by an iron-regulated ubiquitin ligase. *Science* **326**, 718–721 (2009).

14. M. Sanchez, B. Galy, M. U. Muckenthaler, M. W. Hentze, Iron-regulatory proteins limit hypoxia-inducible factor-2alpha expression in iron deficiency. *Nat. Struct. Mol. Biol.* **14**, 420–426 (2007).

15. M. Zimmer, *et al.*, Small-molecule inhibitors of HIF-2a translation link its 5'UTR iron-responsive element to oxygen sensing. *Mol. Cell* **32**, 838–848 (2008).

16. S. A. Anderson, *et al.*, The IRP1-HIF-2α axis coordinates iron and oxygen sensing with erythropoiesis and iron absorption. *Cell Metab.* **17**, 282–290 (2013).

17. M. C. Ghosh, *et al.*, Deletion of iron regulatory protein 1 causes polycythemia and pulmonary hypertension in mice through translational derepression of HIF2α. *Cell Metab.* **17**, 271–281 (2013).

18. N. Wilkinson, K. Pantopoulos, IRP1 regulates erythropoiesis and systemic iron homeostasis by controlling HIF2α mRNA translation. *Blood* **122**, 1658–1668 (2013).

19. P. H. Maxwell, *et al.*, The tumour suppressor protein VHL targets hypoxia-inducible factors for oxygen-dependent proteolysis. *Nature* **399**, 271–275 (1999).

20. V. H. Haase, Regulation of erythropoiesis by hypoxia-inducible factors. *Blood Rev.* **27**, 41–53 (2013).

21. B. Keith, R. S. Johnson, M. C. Simon, HIF1α and HIF2α: sibling rivalry in hypoxic tumour growth and progression. *Nat. Rev. Cancer* **12**, 9–22 (2011).

22. M.-E. Pandelia, N. D. Lanz, S. J. Booker, C. Krebs, Mössbauer spectroscopy of Fe/S proteins. *Biochim. Biophys. Acta* **1853**, 1395–1405 (2015).

23. H. Beinert, R. H. Holm, E. Münck, Iron-sulfur clusters: nature's modular, multipurpose structures. *Science* **277**, 653–659 (1997).

24. P. Gütlich, E. Bill, A. X. Trautwein, *Mössbauer Spectroscopy and Transition Metal Chemistry: Fundamentals and Applications* (Springer-Verlag, 2011) (August 15, 2018).

25. N. Khoroshilova, C. Popescu, E. Münck, H. Beinert, P. J. Kiley, Iron-sulfur cluster disassembly in the FNR protein of Escherichia coli by O2: [4Fe-4S] to [2Fe-2S] conversion with loss of biological activity. *Proc. Natl. Acad. Sci.* **94**, 6087–6092 (1997).

26. S. Ollagnier, *et al.*, Assembly of 2Fe-2S and 4Fe-4S Clusters in the Anaerobic Ribonucleotide Reductase from Escherichia coli. *J. Am. Chem. Soc.* **121**, 6344–6350 (1999).

27. C. A. Royer, Probing Protein Folding and Conformational Transitions with Fluorescence. *Chem. Rev.* **106**, 1769–1784 (2006).

28. P. Haunhorst, C. Berndt, S. Eitner, J. R. Godoy, C. H. Lillig, Characterization of the human monothiol glutaredoxin 3 (PICOT) as iron-sulfur protein. *Biochem. Biophys. Res. Commun.* **394**, 372–376 (2010).

29. C. H. Lillig, *et al.*, Characterization of human glutaredoxin 2 as iron-sulfur protein: a possible role as redox sensor. *Proc. Natl. Acad. Sci. U. S. A.* **102**, 8168–8173 (2005).

30. C. Berndt, *et al.*, How Does Iron Sulfur Cluster Coordination Regulate the Activity of Human Glutaredoxin 2? *Antioxid. Redox Signal.* **9**, 151–157 (2007).

31. C. Johansson, K. L. Kavanagh, O. Gileadi, U. Oppermann, Reversible sequestration of active site cysteines in a 2Fe-2S-bridged dimer provides a mechanism for glutaredoxin 2 regulation in human mitochondria. *J. Biol. Chem.* **282**, 3077–82 (2007).

32. K. Lepka, *et al.*, Iron-sulfur glutaredoxin 2 protects oligodendrocytes against damage induced by nitric oxide release from activated microglia. *Glia* **65**, 1521–1534 (2017).

33. L. Bräutigam, *et al.*, Vertebrate-specific glutaredoxin is essential for brain development. *Proc. Natl. Acad. Sci. U. S. A.* **108**, 20532–20537 (2011).

34. L. Bräutigam, *et al.*, Glutaredoxin regulates vascular development by reversible glutathionylation of sirtuin 1. *Proc. Natl. Acad. Sci. U. S. A.* **110**, 20057–20062 (2013).

35. M. Gellert, *et al.*, The cytosolic isoform of glutaredoxin 2 promotes cell migration and invasion. *Biochim. Biophys. Acta - Gen. Subj.* **1864**, 129599 (2020).

36. C. Wilms, *et al.*, Glutaredoxin 2 promotes SP-1-dependent CSPG4 transcription and migration of wound healing NG2 glia and glioma cells: Enzymatic Taoism. *Redox Biol.* **49**, 102221 (2022).

37. C. Johansson, *et al.*, The crystal structure of human GLRX5: iron-sulfur cluster co-ordination, tetrameric assembly and monomer activity. *Biochem. J.* **433**, 303–311 (2011).

38. C. Berndt, C. H. Lillig, Glutathione, Glutaredoxins, and Iron. *Antioxid. Redox Signal.* **27**, 1235–1251 (2017).

39. N. Rouhier, J. Couturier, M. K. Johnson, J.-P. Jacquot, Glutaredoxins: roles in iron homeostasis. *Trends Biochem. Sci.* **35**, 43–52 (2010).

40. D. Trnka, *et al.*, Molecular basis for the distinct functions of redox-active and FeS-transfering glutaredoxins. *Nat. Commun.* **11**, 3445 (2020).

41. K. Stegmaier, *et al.*, Apd1 and Aim32 Are Prototypes of Bishistidinyl-Coordinated Non-Rieske [2Fe-2S] Proteins. *J. Am. Chem. Soc.* **141**, 5753–5765 (2019).

42. D. Su, C. Berndt, D. E. Fomenko, A. Holmgren, V. N. Gladyshev, A conserved cis-proline precludes metal binding by the active site thiolates in members of the thioredoxin family of proteins. *Biochemistry* **46**, 6903–6910 (2007).

43. F. Zannini, *et al.*, Mitochondrial Arabidopsis thaliana TRXo Isoforms Bind an Iron¯Sulfur Cluster and Reduce NFU Proteins In Vitro. *Antioxid. Basel Switz.* **7** (2018).

44. H. Bisio, *et al.*, A New Class of Thioredoxin-Related Protein Able to Bind Iron-Sulfur Clusters. *Antioxid Redox Signal* (2015) https:/doi.org/10.1089/ars.2015.6377.

45. R. B. Currier, *et al.*, An essential thioredoxin-type protein of Trypanosoma brucei acts as redox-regulated mitochondrial chaperone. *PLoS Pathog.* **15**, e1008065 (2019).

46. A. P. Yeh, *et al.*, Structure of a thioredoxin-like [2Fe-2S] ferredoxin from Aquifex aeolicus. *J. Mol. Biol.* **300**, 587–595 (2000).

47. J.-F. Collet, D. Peisach, J. C. A. Bardwell, Z. Xu, The crystal structure of TrxA(CACA): Insights into the formation of a [2Fe-2S] iron-sulfur cluster in an Escherichia coli thioredoxin mutant. *Protein Sci. Publ. Protein Soc.* **14**, 1863–1869 (2005).

48. C. H. Lillig, C. Berndt, “14:Thioredoxins and Glutaredoxins. Functions and Metal Ion Interactions” in *Metallothioneins and Related Chelators*, (2009), pp. 413–439.

49. E. Soum, *et al.*, Peroxynitrite and nitric oxide differently target the iron-sulfur cluster and amino acid residues of human iron regulatory protein 1. *Biochemistry* **42**, 7648–7654 (2003).

50. X. Brazzolotto, P. Timmins, Y. Dupont, J.-M. Moulis, Structural changes associated with switching activities of human iron regulatory protein 1. *J. Biol. Chem.* **277**, 11995–12000 (2002).

51. C. C. Philpott, D. Haile, T. A. Rouault, R. D. Klausner, Modification of a free Fe-S cluster cysteine residue in the active iron-responsive element-binding protein prevents RNA binding. *J. Biol. Chem.* **268**, 17655–17658 (1993).

52. C. Berndt, J.-D. Schwenn, C. H. Lillig, The specificity of thioredoxins and glutaredoxins is determined by electrostatic and geometric complementarity. *Chem. Sci.* **6**, 7049–7058 (2015).

53. M. Gellert, *et al.*, Substrate specificity of thioredoxins and glutaredoxins - towards a functional classification. *Heliyon* **5**, e02943 (2019).

54. D. J. Haile, Regulation of genes of iron metabolism by the iron-response proteins. *Am J Med Sci* **318**, 230–240 (1999).

55. S. Mueller, Iron regulatory protein 1 as a sensor of reactive oxygen species. *BioFactors Oxf. Engl.* **24**, 171–181 (2005).

56. X. Brazzolotto, J. Gaillard, K. Pantopoulos, M. W. Hentze, J. M. Moulis, Human cytoplasmic aconitase (Iron regulatory protein 1) is converted into its [3Fe-4S] form by hydrogen peroxide in vitro but is not activated for iron-responsive element binding. *J. Biol. Chem.* **274**, 21625–21630 (1999).

57. I. Toth, L. Yuan, J. T. Rogers, H. Boyce, K. R. Bridges, Hypoxia alters iron-regulatory protein-1 binding capacity and modulates cellular iron homeostasis in human hepatoma and erythroleukemia cells. *J. Biol. Chem.* **274**, 4467–4473 (1999).

58. J. B. Goforth, S. A. Anderson, C. P. Nizzi, R. S. Eisenstein, Multiple determinants within iron-responsive elements dictate iron regulatory protein binding and regulatory hierarchy. *RNA N. Y. N* **16**, 154–169 (2010).

59. J.-X. Wang, *et al.*, Oxidative Modification of miR-184 Enables It to Target Bcl-xL and Bcl-w. *Mol. Cell* **59**, 50–61 (2015).

60. C. N. Lok, P. Ponka, Identification of a hypoxia response element in the transferrin receptor gene. *J. Biol. Chem.* **274**, 24147–24152 (1999).

61. S. R. Smith, M. C. Ghosh, H. Ollivierre-Wilson, W. Hang Tong, T. A. Rouault, Complete loss of iron regulatory proteins 1 and 2 prevents viability of murine zygotes beyond the blastocyst stage of embryonic development. *Blood Cells. Mol. Dis.* **36**, 283–287 (2006).

62. E. S. Hanson, E. A. Leibold, Regulation of iron regulatory protein 1 during hypoxia and hypoxia/reoxygenation. *J. Biol. Chem.* **273**, 7588–7593 (1998).

63. E. S. Hanson, L. M. Foot, E. A. Leibold, Hypoxia post-translationally activates iron-regulatory protein 2. *J. Biol. Chem.* **274**, 5047–5052 (1999).

64. T. Christova, D. M. Templeton, Effect of hypoxia on the binding and subcellular distribution of iron regulatory proteins. *Mol. Cell. Biochem.* **301**, 21–32 (2007).

65. M. R. Pawlus, C.-J. Hu, Enhanceosomes as integrators of hypoxia inducible factor (HIF) and other transcription factors in the hypoxic transcriptional response. *Cell. Signal.* **25**, 1895–1903 (2013).

66. E. Pourcelot, *et al.*, The iron regulatory proteins are defective in repressing translation via exogenous 5’ iron responsive elements despite their relative abundance in leukemic cellular models. *Met. Integr. Biometal Sci.* **10**, 639–649 (2018).

67. J. R. Godoy, *et al.*, Redox atlas of the mouse. Immunohistochemical detection of glutaredoxin-, peroxiredoxin-, and thioredoxin-family proteins in various tissues of the laboratory mouse. *Biochim. Biophys. Acta* **1810**, 2–92 (2011).

68. A. Janoschka, G. Svenconis, V. Schünemann, A closed cycle-cryostat for high-field Mössbauer spectroscopy. *J. Phys. Conf. Ser.* **217**, 012005 (2010).

69. H. P. Gunnlaugsson, Spreadsheet based analysis of Mössbauer spectra. *Hyperfine Interact.* **237**, 79 (2016).

70. V. Schünemann, H. Winkler, Structure and dynamics of biomolecules studied by Mössbauer spectroscopy. *Rep. Prog. Phys.* **63**, 263 (2000).

71. H. Montgomery, B. Morosin, J. J. Natt, A. M. Witkowska, E. C. Lingafelter, The crystal structure of Tutton's salts. VI. Vanadium(II), iron(II) and cobalt(II) ammonium sulfate hexahydrates. *Acta Crystallogr.* **22**, 775–780 (1967).

72. G. Jander, E. Blasius, *Lehrbuch der analytischen und präparativen anorganischen Chemie: mit 45 Tabellen*, 14., neu bearb. Aufl. / von Joachim Strähle und Eberhard Schweda (Hirzel, 1995).

73. A. Biederbick, *et al.*, Role of human mitochondrial Nfs1 in cytosolic iron-sulfur protein biogenesis and iron regulation. *Mol. Cell. Biol.* **26**, 5675–5687 (2006).

74. E. S. Arnér, A. Holmgren, Measurement of thioredoxin and thioredoxin reductase. *Curr. Protoc. Toxicol.* **Chapter 7**, Unit 7.4. (2001).

75. P. Haunhorst, *et al.*, Crucial function of vertebrate glutaredoxin 3 (PICOT) in iron homeostasis and hemoglobin maturation. *Mol. Biol. Cell* **24**, 1895–1903 (2013).

76. S. Stöcker, M. Maurer, T. Ruppert, T. P. Dick, A role for 2-Cys peroxiredoxins in facilitating cytosolic protein thiol oxidation. *Nat. Chem. Biol.* **14**, 148–155 (2018).

77. K. Brenig, *et al.*, The Proteomic Landscape of Cysteine Oxidation That Underpins Retinoic Acid-Induced Neuronal Differentiation. *J. Proteome Res.* **19**, 1923–1940 (2020).

78. N. Guex, M. C. Peitsch, SWISS-MODEL and the Swiss-PdbViewer: an environment for comparative protein modeling. *Electrophoresis* **18**, 2714–2723 (1997).

79. T. Schwede, J. Kopp, N. Guex, M. C. Peitsch, SWISS-MODEL: An automated protein homology-modeling server. *Nucleic Acids Res.* **31**, 3381–3385 (2003).

80. M. Wiederstein, M. J. Sippl, ProSA-web: interactive web service for the recognition of errors in three-dimensional structures of proteins. *Nucleic Acids Res.* **35**, W407-410 (2007).

81. D. Van Der Spoel, *et al.*, GROMACS: fast, flexible, and free. *J. Comput. Chem.* **26**, 1701–1718 (2005).

82. K. Lindorff-Larsen, *et al.*, Improved side-chain torsion potentials for the Amber ff99SB protein force field. *Proteins* **78**, 1950–1958 (2010).

83. A. T. P. Carvalho, A. F. S. Teixeira, M. J. Ramos, Parameters for molecular dynamics simulations of iron-sulfur proteins. *J. Comput. Chem.* **34**, 1540–1548 (2013).

84. B. Hess, H. Bekker, H. Berendsen, J. Fraaije, LINCS: A Linear Constraint Solver for molecular simulations. *J. Comput. Chem.* **18**, 12 (1998).

85. M. Parrinello, A. Rahman, Polymorphic transitions in single crystals: A new molecular dynamics method. *J. Appl. Phys.* **52**, 7182–7190 (1981).

86. G. Bussi, D. Donadio, M. Parrinello, Canonical sampling through velocity rescaling. *J. Chem. Phys.* **126**, 14101–14101 (2007).

87. T. Darden, D. York, L. Pedersen, Particle mesh Ewald: An N· log(N) method for Ewald sums in large systems. *J. Chem. Phys.* **98**, 10089–10092 (1993).

88. E. F. Pettersen, *et al.*, UCSF Chimera--a visualization system for exploratory research and analysis. *J. Comput. Chem.* **25**, 1605–1612 (2004).

Tables

Table 1 Mössbauer parameters of reconstituted holo-Trx1.

Holo-Trx1 was reconstituted *in vitro* and concentrated to 2.5 mM. The protein was frozen in liquid nitrogen and analyzed by Mössbauer spectroscopy at 77 K as outlined in the experimental procedures, see also Fig. 1.

parameter	fraction 1	fraction 2
	without external magnetic field	
δ (mm s^{-1})	0.35 ± 0.02	0.56 ± 0.02
ΔE_Q (mm s^{-1})	0.66 ± 0.03	0.72 ± 0.03
Γ (mm s^{-1})	0.33 ± 0.03	0.43 ± 0.03
area (%)	22 ± 2	78 ±2

Figures

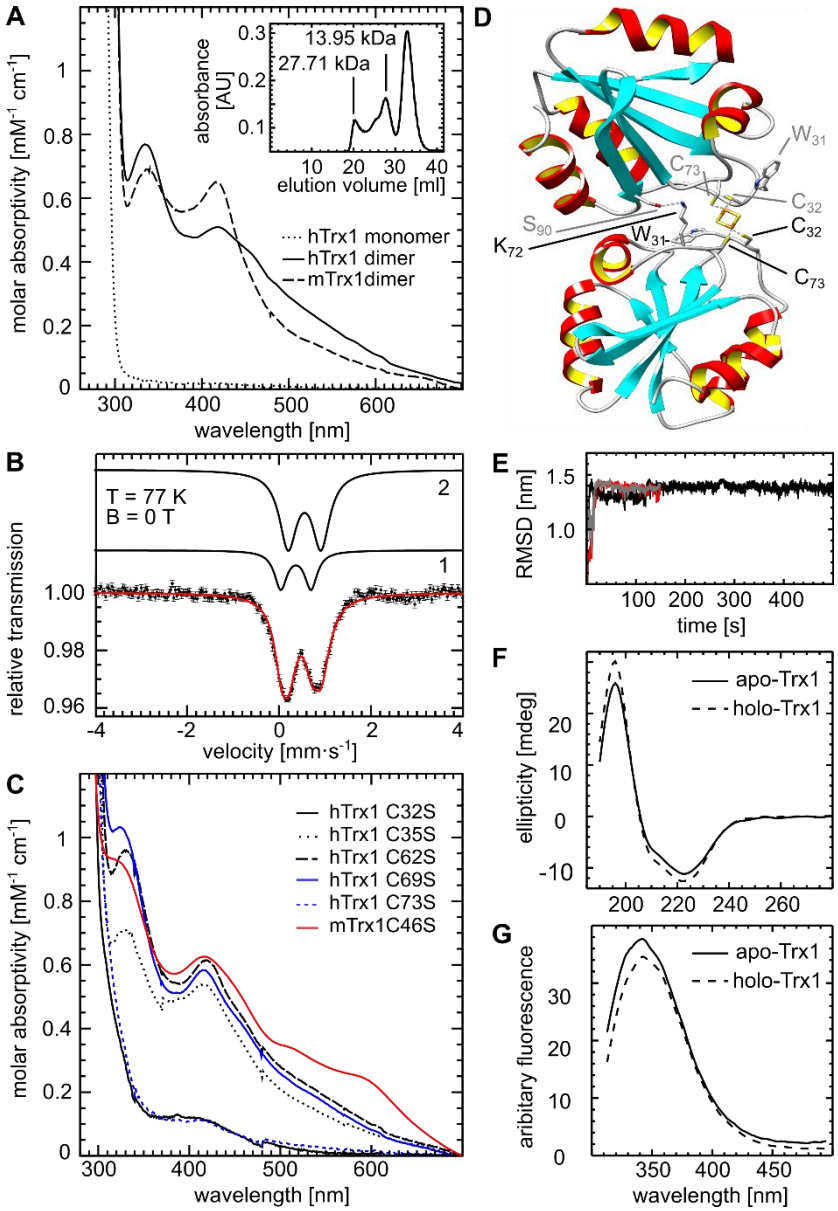

Figure 1 Identification of a [2Fe-2S]$^{2+}$ cluster in human and mouse Trx1. A) UV-Vis spectroscopy of recombinantly expressed monomeric and dimeric human Trx1 and mouse Trx1 after purification. The spectra of the human Trx1 correspond to the fractions separated by gelfiltration shown in the inset. Inset: Chromatogram of the gelfiltration chromatography separating monomeric apo-Trx1 and dimeric holo-Trx1. B) Mössbauer spectra of reconstituted human Trx1 obtained at 77 K. The simulated spectra of fractions 1 and 2 (see text and table 1) were included on top of the recorded spectra. C) UV-Vis spectroscopy after purification of recombinant human and mouse Trx1 with individually

mutated cysteinyl residues as indicated. D) Model of the holo-Trx1 complex after MD simulation (the most representative structure is shown). The FeS ligands and two amino acids stabilizing the dimer are highlighted. E) Root mean square deviations (RMSD) of the backbone of holo-Trx1 complex while three independent molecular dynamics simulations F-G) CD spectra (F) and fluorescence spectra at 294 nm excitation (Trp fluorescence, G) of monomeric apo-Trx1 and dimeric holo-Trx1 after gel filtration chromatography.

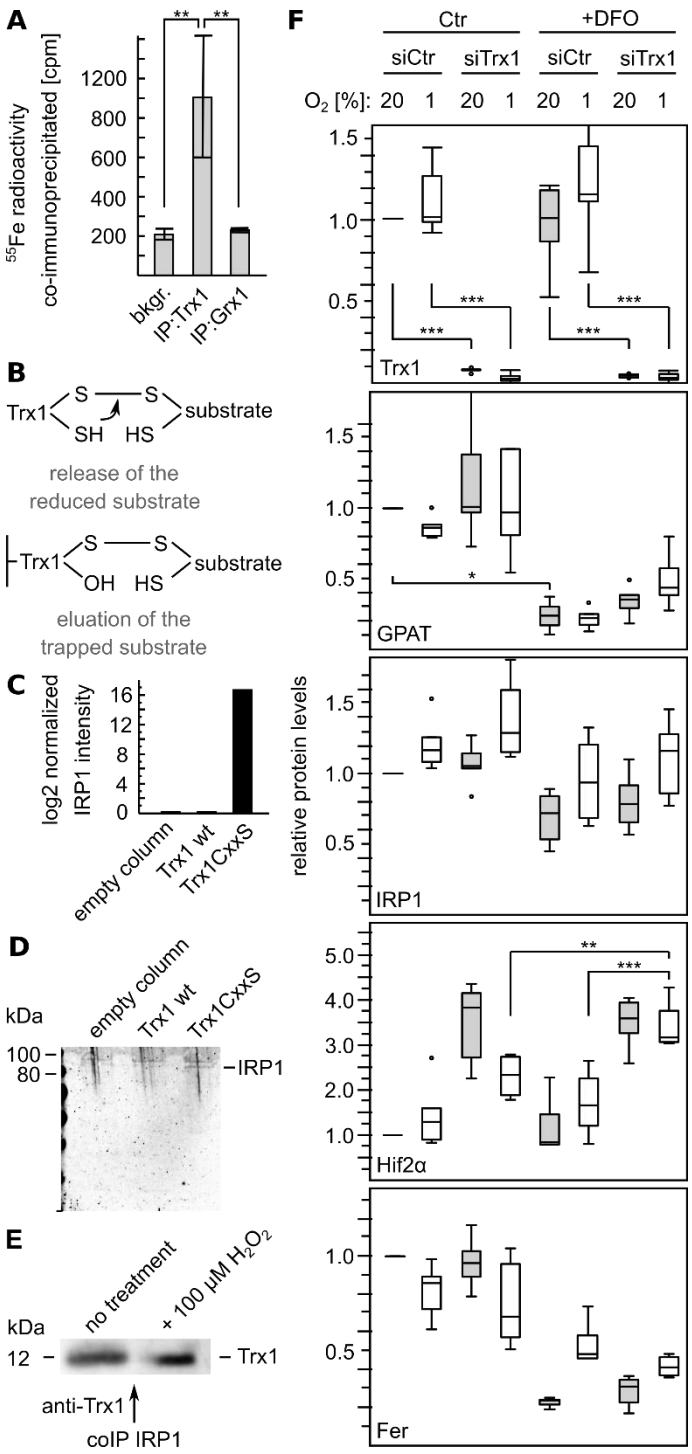

Figure 2 Trx1 interacts with IRP1 and affects the response on iron-depletion and hypoxia. A) Co-immunoprecipitation of ^{55}Fe with Trx1 from Jurkat cell extracts propagated with transferrin-bound ^{55}Fe as main iron source (n=3, mean ± SD). B) Schematic mechanism of substrate trapping by a column coupled Trx1 mutant. C)-D) Identification of IRP1 as substrate of Trx1 using HeLa cell extracts. C) Quantification of IRP1 peptides via mass spectrometry in the eluted interaction partners. D) Identification of IRP1 as substrate

after Western blotting of the eluted trapped substrates. E) Co-immunoprecipitation using anti-IRP1 antibodies revealed Trx1 as interacting protein in Jurkat cells ± H_2O_2 treatment after Western blotting. F) Analysis of the protein levels of Trx1, glutamine phosphoribosylpyrophosphate amidotransferase (GPAT), iron regulatory protein 1 (IRP1), hypoxia-induced factor 2α (HIF2α), and ferritin (Fer) in control cells (siCtr) and cells depleted of Trx1 by siRNA treatment (siTrx1). These cells were cultivated with or without the iron chelator deferoxamine (DFO) under 20 % or 1 % oxygen to induce both, iron-limiting and hypoxic conditions. The box plots depict the medians as center lines; box limits indicate the 25th and 75th percentiles as determined by R software; whiskers extend 1.5 times the interquartile range from the 25th and 75th percentiles, outliers are represented by dots (n = 6, *: $p<0.05$, **: $p<0.01$, ***: $p<0.001$, Students T-test).

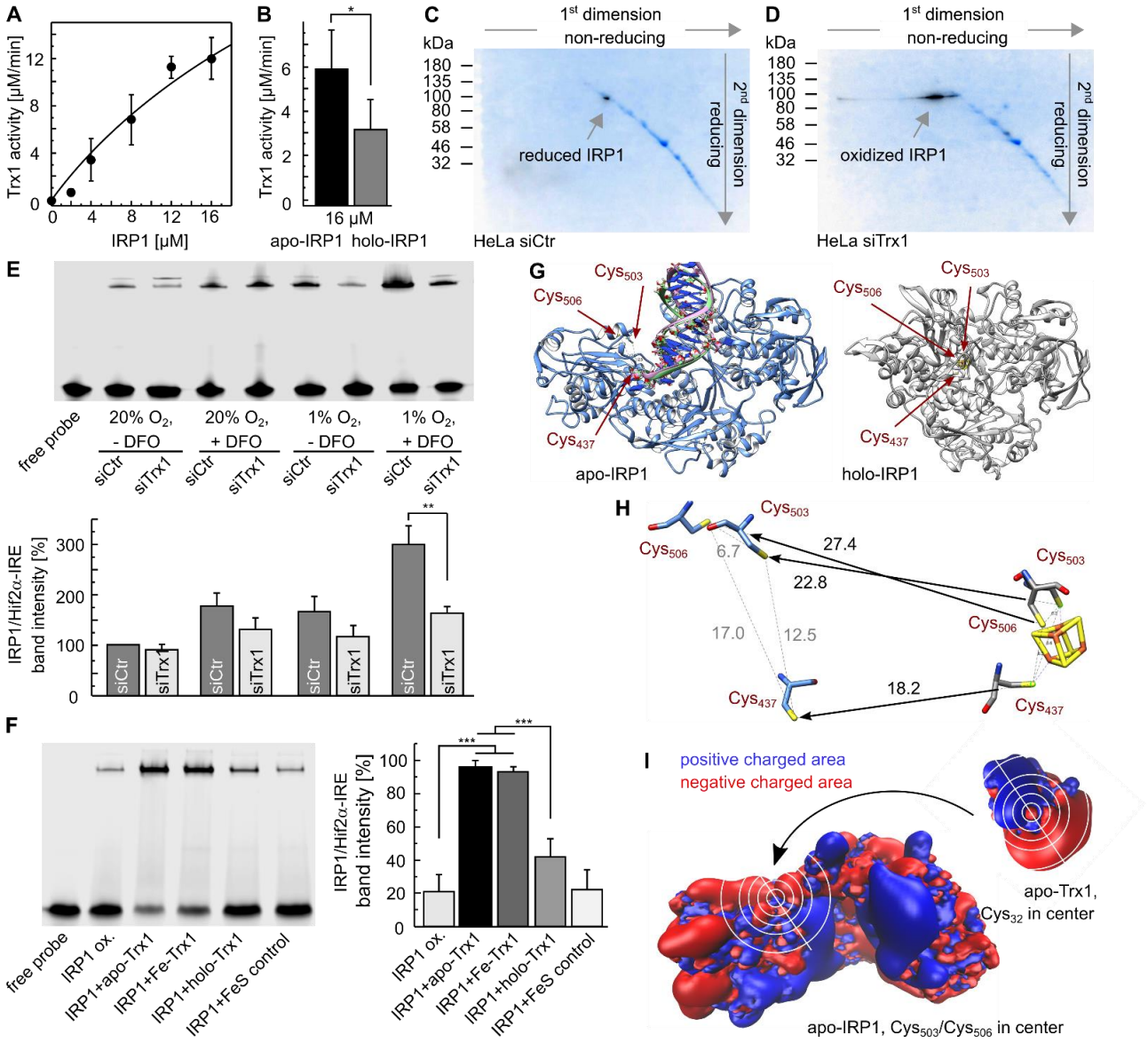

Figure 3 Trx1 reduces IRP1 and regulates IRP1 binding to Hif2α-IRE. A) Reduction of different concentrations of recombinant IRP1 as indicated by Trx1 *in vitro* in a coupled kinetic assay with rat TrxR1 and NADPH measuring NADPH consumption at 340 nm. The solid line is a non-linear curve fitting of the data points (n = 4, mean ± SD) to the Michaelis-Menten equation. B) Using the same assay as in A), holo- and apo-IRP1 were used as substrates. The assay was performed under anaerobic conditions (n = 3, mean ± SD). C-D) Diagonal 2-dimensional SDS PAGE under non-reducing (first dimension) and reducing conditions (second dimension) reveals the redox state of IRP1 in control (C) and Trx1-

depleted HeLa cells (D) cultivated at 1% O_2 in the presence of deferoxamine (DFO). The pictures show overlays of the total amount of proteins in blue (Coomassie staining) and a Western blot staining of IRP1 in black. E) Electrophoretic shift assays (EMSAs) with extracts of HeLa cells cultivated under 20 % or 1 % O_2, ± iron chelator deferoxamine (DFO), and ± Trx1 depletion (siTrx1 or siCtr). Extracts were mixed with infrared-labeled Hif2α-IRE probe to determine RNA binding capacity of IRP1 (n = 6-14, mean ± SEM, **: $p<0.001$, Students T-test). F) Recombinant IRP1 was incubated with apo-Trx, holo-Trx (after *in vitro* reconstitution), Trx-Fe (Trx1 incubated with $(NH_4)_2Fe(SO_4)_2$), and FeS control mixture (*in vitro* reconstitution mixture without Trx1) in presence of a labeled Hif2α-IRE probe to perform an EMSA Quantification shows mean ± SEM (n = 3-11, **: $p<0.01$, ***: $p<0.001$, Students T-test). G) Model structure of apo-IRP1 with bound IREs (left blue structure based on pdb codes 3sn2 and 3snp) and holo-IRP1/Aconitase (right grey structure based on pdb code 2b3x). H) Orientation, distances, and movements (arrows) of cysteinyl residues 437, 503, and 506 during apo to holo transition. I) Electrostatic isosurfaces of apo-IRP1 and hTrx1 at ± 25 mV display complementary binding surfaces.

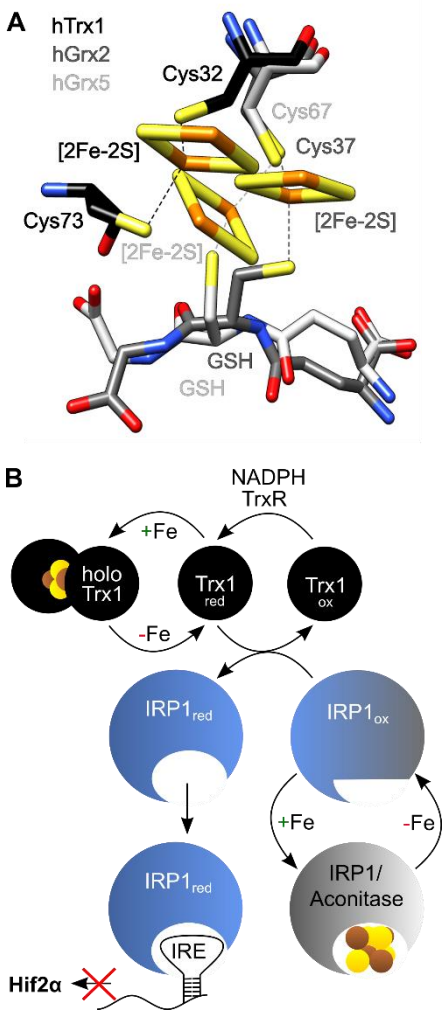

Figure 4 FeS cluster coordination in Trx family proteins. A) Alignment of the structures of human holo-Grx2 (pdb entry: 2ht9), holo-Grx5 (2wul), and holo-Trx1 (obtained by modeling in this study) depicting the position of the thiol groups recruited for binding of the [2Fe-2S] clusters. The FeS clusters bound to Grx2 and Grx5 were included in the image. B) Model for the activation of Trx1 and IRP1 by FeS cluster disassembly and redox regulation, for details see text.

Supplementary Information

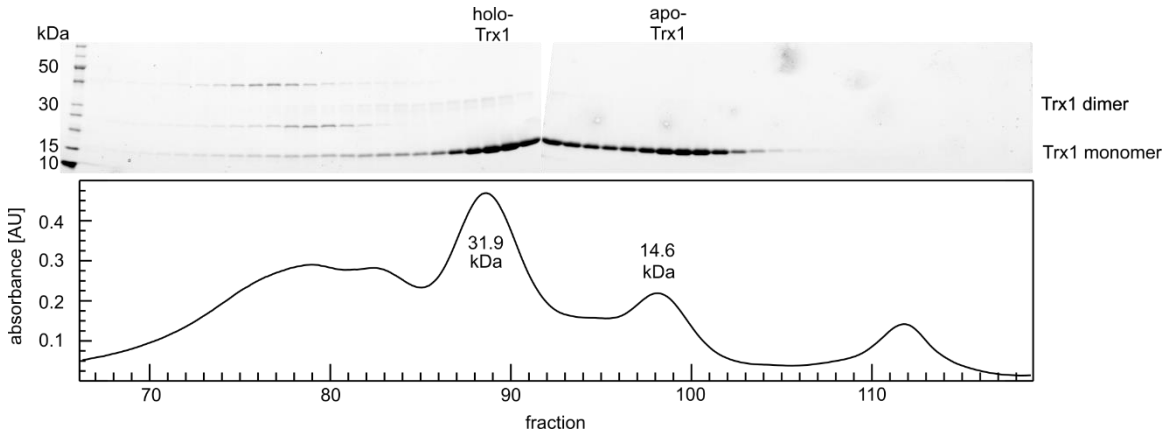

Fig. S1 Mouse Trx1 forms dimers and monomers after *in vitro* reconstitution and is the main/single protein in the respective gelfiltration peaks. Reconstituted mTrx1 was applied to gelfiltration. The peaks fit to the theoretical MW of mTrx1 monomer (13.84 kDa) and dimer (27.76 kDa). The corresponding gels demonstrate that purified Trx1 is the only protein in these two peak fractions and thereby the protein leading to the recorded spectra.

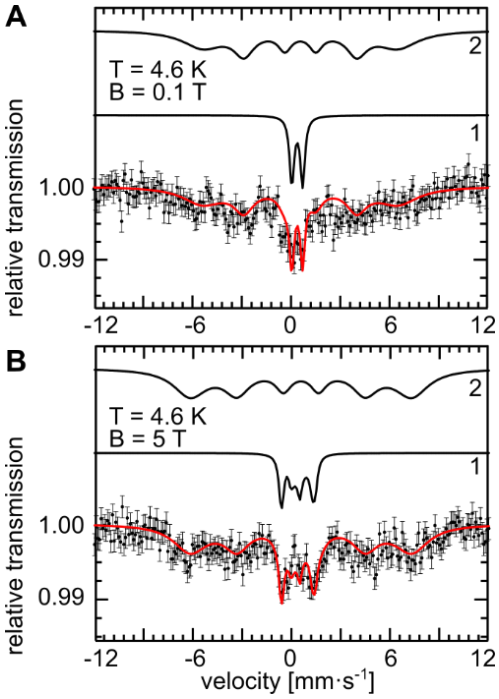

Fig. S2 Mössbauer spectra of reconstituted human Trx1 obtained at 4.6 K in the presence of external magnetic fields. A) 0.1 T, B) 5 T. The field direction was parallel to the γ-ray. The simulated spectra of fractions 1 and 2 (see text and Tab. S1) were included on top of the recorded spectra.

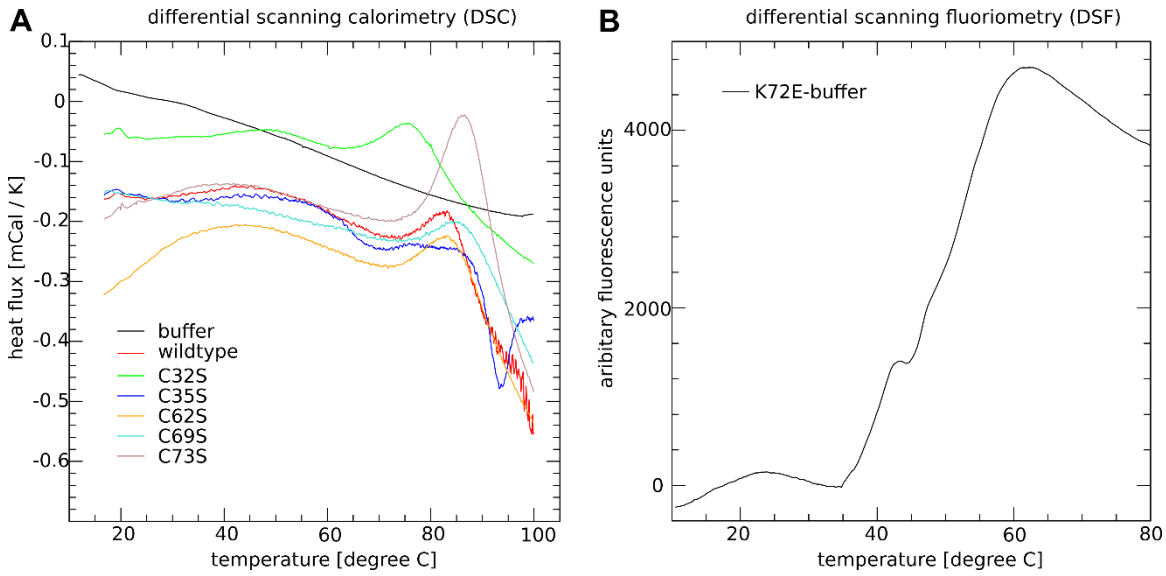

Fig. S3 Thermal stability of the recombinantly expressed Trx1 mutants. A) Differential scanning calorimetry: The recombinant proteins at 40 µM in PBS buffer were heated at 1 K per minute from 20 to 100°C. The resulting heat flux was recorded. In all cases, denaturation started above 70°C, for the T_m see peaks. B) Differential scanning fluorimetry: The recombinant protein at 10 µM in PBS buffer was heated at 0.2 K per minute from 20 to 80 °C in the presence of sypro orange. Here, the T_m corresponds to the center of the increasing part of the curve, it was determined by fitting the data to the Boltzmann equation (see Methods section). The thermal stability of wild-type Trx1 determined here was lower compared to previous studies (see for instance [SI1]). This was likely caused by the use of different buffer systems and the use of His-tagged proteins in our study. The calculated denaturation temperatures of the Trx1 mutants are summarized in table S2.

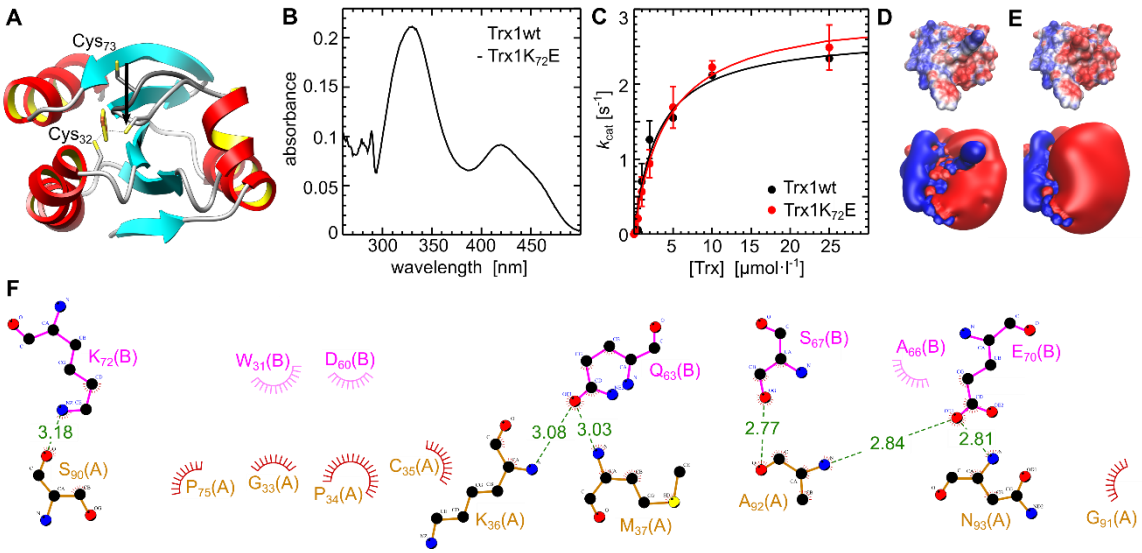

Fig. S4 Conformational changes in human Trx1 upon binding of the iron cofactor. A) Conformational changes in the loop containing Cys73 required for FeS cluster ligation (dark gray apo-Trx1, light gray holo-Trx1). The arrow represents app. 6-7 Å. B) Difference UV-Vis spectra between wildtype and K72E Trx1 demonstrates the lack in [2Fe-2S] absorptivity in the mutant. C) Michaelis-Menten plot of TrxR1 activity with Trx1wt and Trx1K72E as substrate in a coupled assay with insulin to keep Trx1 in the oxidized state (n=6, mean ± SD). D-E) Electrostatic surface potential (upper panel) from -100 to +100 mV and elelctrostatic isosurfaces at +/- 25 mV of the K72E mutant (D) and wildtype protein (E). F) DimPlot showing the interaction between the two Trx1 monomers in a dimer (dashed lines: hydrogen bonds, arcs: hydrophopic contacts). The plot is based on a representative frame of the MD simulations.

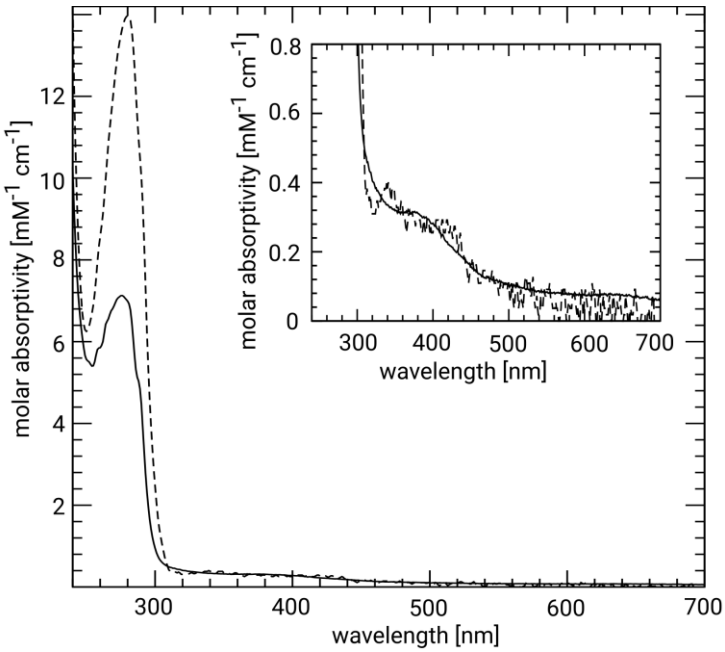

Fig. S5 *E. coli* Trx1 and human Trx2 are not FeS cluster proteins. UV-Vis spectra of *E. coli* Trx1 (dashed line) and human Trx2 (straight line). The proteins were expressed and purified in the same way as human and mouse Trx1. *E.c.*Trx1 was cloned into the expression vector pET15b using the restriction sites NdeI and BamHI and the following primers: fwd: 5' CACACACATATGAGCGATAAAATTATTCACCTGACTGACGACAG and rev: 5' CACACAGGATCCTTACGCCAGGTTAGCGTCGAGGAAC. Construction of the mTrx2 plasmid is described in [SI2].

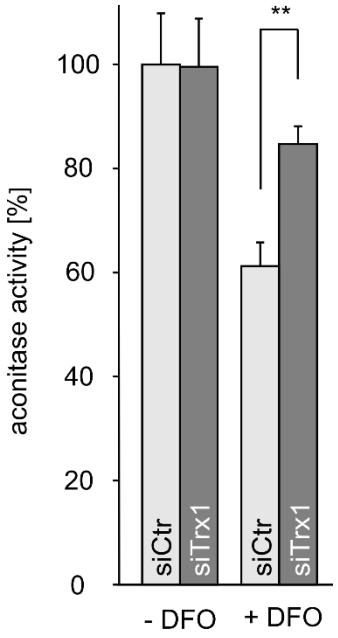

Fig. S6 Trx1 deficiency increases aconitase activity. Cytosolic aconitase activity of control and Trx1-depleted HeLa cells cultivated under 1 % O_2 in the presence and absence of DFO (n=3, mean ± SD, **: $p<0.01$, Students T-test).

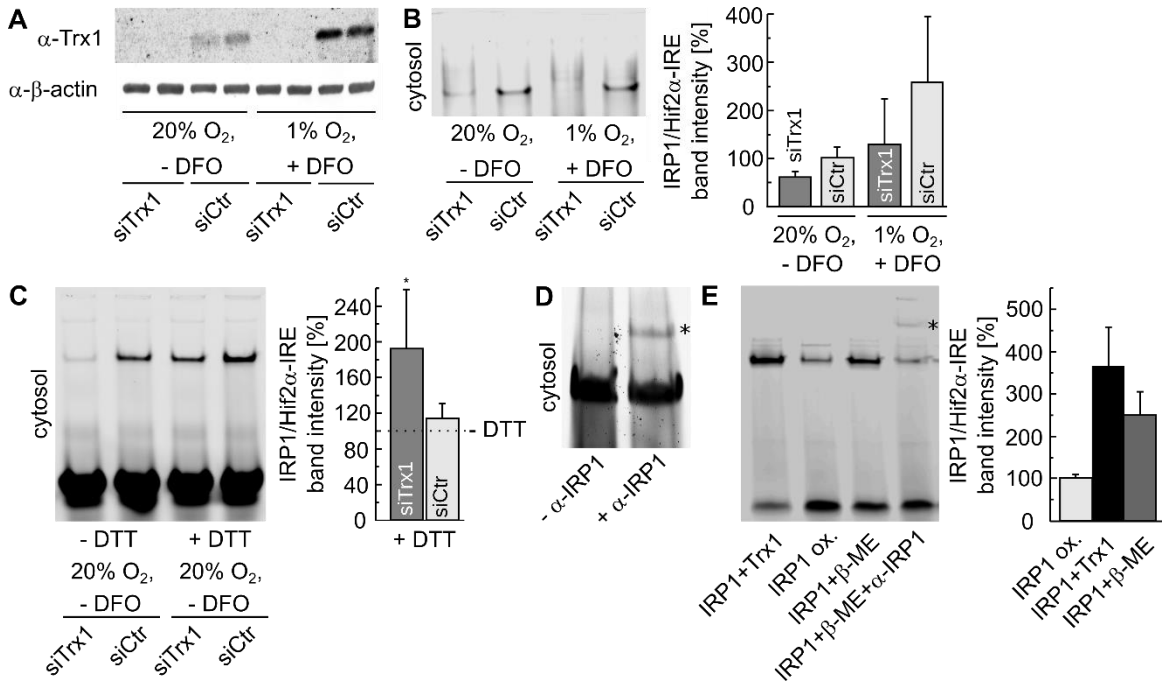

Fig. S7 Electrophoretic mobility shift assays (EMSAs) using a Hif2α-IRE probe. A) Successful knock-out of Trx1 via siRNA in the HeLa cells used for the EMSAs. B) EMSAs of cytosolic fractions of HeLa cells ± hypoxic (1 % O_2) and iron-limiting (+ iron chelator desferoxamine (DFO)) conditions ± Trx1 depletion (siTrx1). n = 3, mean ± SEM. C) Cytosolic fractions of HeLa cells grown as indicated were treated with or without 300 mM DTT before EMSA. n = 5, mean ± SEM, *: $p<0.05$, Students T-test. D) Formation of a supershift complex (asterisk) consisting of probe, IRP1, and anti-IRP1 antibodies in cytosolic fractions of HeLa cells propagated under 1 % O_2 + DFO and electroporated with control siRNA. E) Recombinant IRP1 was incubated ± recombinant apo-Trx1 (10 µM) or ± β-mercaptoethanol (β-ME, 10 mM) with or without presence of anti-IRP1 antibodies for the formation of superhift complexes (asterisk) (n = 3-4, mean ± SEM).

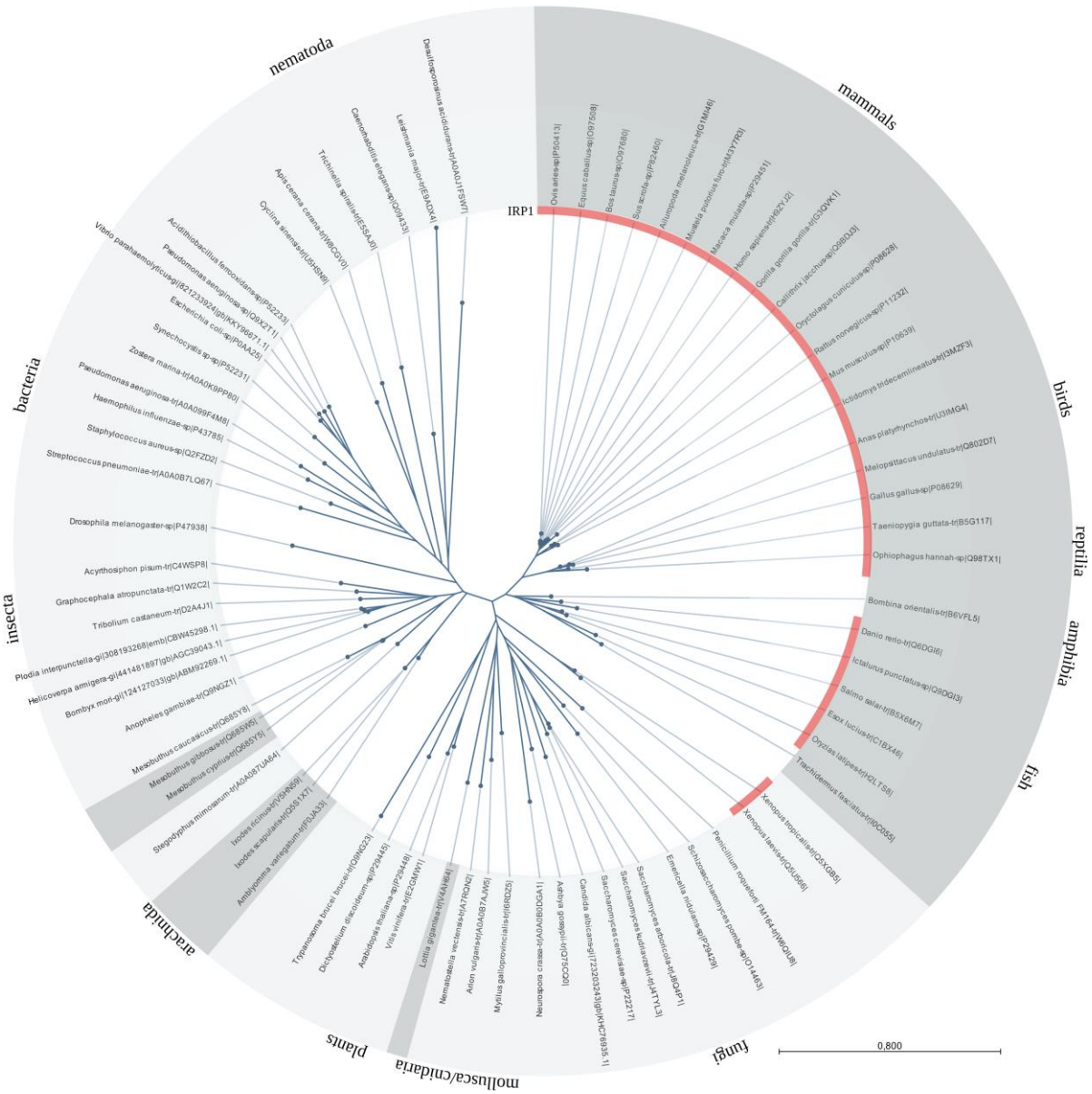

Fig. S8 Phylogeny of Trx1 homologues. We have performed sequence comparison between Trxs from various species, classes, and kingdoms. All species contain the active site motif CxxC. The radial phylogenic tree shows the species that contain the extra Cys73 essential for FeS coordination (highlighted in grey); mainly vertebrates, arachnid species and one mollusk. The figure also includes the species in which IRP1 has been identified (depicted in red). Alignments and the radial phylogenetic tree were created using the CLC Sequence Viewer 8.

Table S1 Mössbauer parameters of reconstituted holo-Trx1 obtained at 4.6 K in presence of external magnetic fields. Holo-Trx1 was reconstituted *in vitro* and concentrated to 2.5 mM. The protein was frozen in liquid nitrogen and analyzed by Mössbauer spectroscopy as outlined in the experimental procedures, see also Fig. S2. Fraction 1 was simulated by means of the spin-Hamiltionian formalism assuming a diamagnetic (S = 0) ground state [SI3].

parameter	fraction 1	fraction 2
	S=0	
δ (mm s^{-1})	0.35 ± 0.02	0.56 ± 0.10
ΔE_Q (mm s^{-1})	0.66 ± 0.03	0
η	0 ± 0.5	-
$\Gamma_{(5T)}$ (mm s^{-1})	0.33 ± 0.03	2.5/1.9/1.2 ± 0.50
$\Gamma_{(0,1T)}$ (mm s^{-1})	0.33 ± 0.03	3/1.5/1 ± 0.50
$B_{HF(5T)}$ (T)	-	42 ± 1
$B_{HF(0,1T)}$ (T)	-	37 ± 1
area (%)	20 ± 2	80 ± 2

Table S2 Denaturation temperatures of the Trx1 mutants. The temperatures where half of the proteins were found to be denatured was extracted from Fig. S3.

protein	denaturation temperature °C
human Trx1 wildtype	82.8
human Trx1 C32S	75.6
human Trx1 C35S	83.5
human Trx1 C62S	83.5
human Trx1 C69S	85.4
human Trx1 C73S	86.3
human Trx1 K72E	49.7

SI References

SI1 J.M. Louis, R.E. Georgescu, M.L. Tasayco, O. Tcherkasskaya, A.M. Gronenborn, Probing the structure and stability of a hybrid protein: the human-E. coli thioredoxin chimer. *Biochemistry* **40**:311184-92 (2001)

SI2 E.-M. Hanschmann *et al*., Both thioredoxin 2 and glutaredoxin 2 contribute to the reduction of the mitochondrial 2-Cys peroxiredoxin Prx3. *J. Biol. Chem.* **285**: 40699-705 (2010)

SI3 V. Schünemann, H. Winkler, Structure and dynamics of biomolecules studied by Mössbauer spectroscopy. *Rep. Prog. Phys*. **63**, 263-353 (2000)